

# Pure shear plastic flow and failure of titanium alloys under quasi-static and dynamic torsional loading

Longhui Zhang<sup>\*</sup>, David Townsend, Antonio Pellegrino, Nik Petrinic

Department of Engineering Science, University of Oxford, Parks Road, Oxford, OX1 3PJ, UK

## ARTICLE INFO

### Keywords:

Titanium alloys  
Pure shear  
Constitutive behavior  
Strain localization  
Hopkinson bar

## ABSTRACT

The pure shear responses of Ti6Al4V alloy and Ti3Al2.5V alloy, conceived for unique applications in jet engine components, are compared using Digital Image Correlation technique from quasi-static ( $10^{-3}$ /s), medium strain rate ( $10^1$ /s) and high strain rates ( $10^3$ /s). A series of bespoke torsion tests have been performed on a screw driven mechanical system, a fast hydraulic Instron machine and a Campbell split Hopkinson torsion bar, equipped with high speed photographic equipment. Observations have provided the strain rate dependence and the relation of pure shear failure at quasi-static and high strain rates. The quasi-static shear constitutive relationships including shear modulus, yield stress and failure strain of both alloys are compared at the location of failure initiation, using a bespoke four camera system. The Ti3Al2.5V alloy presents lower shear flow stress and strain rate sensitivity with higher ductility, as opposed to the Ti6Al4V alloy with limited plastic deformation capacity. Associated with modest estimated overall temperature rise until final collapse of the specimen, both ductile Ti3Al2.5V alloy and brittle Ti6Al4V alloy fail by adiabatic shear banding at high strain rates. This is different from the void growth induced failure at medium strain rate with mild temperature rise and at quasi-isothermal condition. The present results show a general description of brittle and ductile alloys in engineering design. Likewise, this study will guide the characterization of pure shear flow and failure for current and future developed impact resistant alloys.

## 1. Introduction

Titanium (Ti) alloys with the combination of light weight, high strength, outstanding resistance to corrosion have been widely employed in jet engine applications (Leyens and Peters, 2003). The bird strike and the blade off events would threaten these critical aircraft structures and materials in service, in which the jet engine components are subjected to intensive impact loading. It is essential to adopt the dynamic constitutive response of materials to analyze the impact events.

The split Hopkinson compression bar (SHPB) technique has been popularly used in the characterization of dynamic stress-strain relationship of engineering materials under uniaxial stress condition (Hopkinson, 1914; Kolsky, 1949). However, the complication of the SHPB experiment arises from Poisson's ratio induced radial expansion of the specimen (Espinosa et al., 2000; Li et al., 2009; Lu et al., 2015; Yang and Song, 1985). The expansion results in a radial stress superposed on the axial stress component. Meanwhile, due to the frictional contact condition at the loaded surfaces, the radial motion causes the barreling of the specimen (Siviour and Walley, 2018). This results in a frictional

shear stress superposed on the axial stress component. The above difficulties experienced in the SHPB tests can be eliminated by using the Torsional Split Hopkinson Bar (TSHB) (Baker and Yew, 1966). Shortly after Campbell and Dowling (1970), Lewis and Campbell (1972), Duffy et al. (1971), Nicholas and Campbell (1972) worked together to improve the generation of torsional wave and laid out the foundations of the TSHB apparatus nowadays. With the absence of radial motion in dynamic torsion tests, the radial inertial effect and the friction effect are avoided. The torsion tests provide a pure stress state to reveal the inherent dynamic plastic flow response of a material. Meanwhile, the last decade has seen the popular applications of Digital Image Correlation (DIC) with non-contact characteristics for full-field strain measurements (Daly et al., 2009; Tzibula et al., 2018; Yang et al., 2014; Zhang et al., 2020a). The combined modern high speed DIC and TSHB techniques would be desirable to measure the torsional constitutive response at high strain rates.

Shear plastic deformation and failure of titanium alloys for jet engine components under impact are important considerations for industry engineers. Although showing encouraging ballistic performances, Ti

<sup>\*</sup> Corresponding author.

E-mail addresses: [lhzhang.mechanics@gmail.com](mailto:lhzhang.mechanics@gmail.com), [longhui.zhang@eng.ox.ac.uk](mailto:longhui.zhang@eng.ox.ac.uk) (L. Zhang).

alloys are very sensitive to dynamic shear failure, which consists of intense shear strain localization (Dodd and Bai, 2012; Walley, 2007; Winter, 1975) associated with adiabatic temperature rise due to thermomechanical coupling effect. Specifically, a certain portion of plastic strain energy converts to heat and raise the temperature in dynamically deforming materials under adiabatic (or nearly) conditions, a subject that was first investigated by Tresca (1879), Farren and Taylor (1925), Taylor and Quinney (1934), and by Rittel (1999); Rittel et al. (2009); Rittel et al. (2017b) in the recent decades.

To investigate the thermomechanical coupling response of titanium alloys, Macdougall and Harding (1998) characterized the dynamic pure shear stress-strain relationship of Ti6Al4V alloy using the Campbell (or Duffy) Hopkinson torsion bar and measured the adiabatic temperature rise using transient infrared thermometry technique. Almost at the same time, a series of dynamic torsional experiments were carried out by Liao and Duffy (1998) focusing on the adiabatic temperature during shear localization in Ti6Al4V alloy. Based on the TSHB technique and pyrometry technique, Ranc et al. (2008) also studied the adiabatic temperature evolution in dynamically deforming Ti6Al4V alloy, in order to understand the mechanisms of initiation and propagation of adiabatic shear band. A modified TSHB was recently designed by Yang et al. (2014) for the investigation of dynamic interrupted shear stress-strain relations and the corresponding frozen microstructures of Ti6Al4V alloy. Zhang et al. (2018) investigated the shear compressive response and the corresponding adiabatic temperature rise of several aircraft structural titanium alloys such as near  $\alpha$  Ti3Al2.5V alloy. The thermomechanical coupled shear behavior was successfully characterized by using a shear compression specimen (SCS) (Dorogoy et al., 2015; Rittel et al., 2002, 2017a), based on the SHPB technique synchronized with a high-speed infrared detector. The SCS specimen was also used by Longère and Dragon (2015) to investigate the mechanism at the origin of the shear failure of Ti6Al4V alloy at quasi-static and high strain rates. Verleysen and Peirs (2017) compared the in-plane shear and pure shear fracture behavior of Ti6Al4V alloy using sheet and thin-walled tube specimens at quasi-static and high strain rates. From this literature review, one can find that most dynamic torsion tests were solely for Ti6Al4V alloy. However, the comparison of torsional flow and failure of titanium alloys is less reported. The available pure shear studies of titanium alloys were mainly either at high strain rates or under quasi-static condition. Consequently, there is a lack of test data in the strain rate gap between quasi-static and high strain rates. This is important to provide more information about the strain rate dependence and the (missing) relation of pure shear failure between quasi-static and high strain rates. Likewise, the comparison of the torsional constitutive relationship and failure of titanium alloys across a wide range of strain rates is seldom investigated.

In the present paper, complemented by DIC, the bespoke torsion techniques (Zhang et al., 2021) are employed to compare the pure shear flow and failure of Ti6Al4V alloy and Ti3Al2.5V alloy from quasi-static, medium to high strain rates. Here, the quasi-static and high strain rate correspond to strain rates at the level of  $10^{-3}/s$  and  $10^3/s$ , while the medium strain rate is about  $10^1/s$ . Ti6Al4V alloy and Ti3Al2.5V alloy were chosen due to their unique applications (similar to spear and shield) in jet engine components. A comparison of torsional response of these two titanium alloys will benefit the design of jet engine components. This study will also guide the development of new impact resistant titanium alloys. The paper is therefore organized as follows: Section 2 introduces the materials, torsion specimen and the experimental setups. Section 3 reports the experimental results at various strain rates. The next section is the discussion of the experimental data, followed by the conclusions.

## 2. Materials and methods

### 2.1. Materials

The materials investigated are Grade 5 Ti6Al4V alloy and Grade 9

**Table 1**

Chemical compositions of Ti6Al4V and Ti3Al2.5V alloys (wt%).

| Material  | Ti       | Al | V   | O    | Fe   | C    | H     | N    |
|-----------|----------|----|-----|------|------|------|-------|------|
| Ti6Al4V   | Balanced | 6  | 4   | 0.20 | 0.25 | 0.08 | 0.015 | 0.05 |
| Ti3Al2.5V | Balanced | 3  | 2.5 | 0.15 | 0.25 | 0.08 | 0.015 | 0.03 |

Ti3Al2.5V alloy. Compared to the high strength Ti6Al4V alloy, the near  $\alpha$  Ti3Al2.5V alloy is usually referred to as 'half 6–4', which offers lower strength but is more formable to machine to various complex shapes. Table 1 gives the chemical compositions of these two alloys.

### 2.2. Microstructural characterization

After being prepared following standard procedure and polished by 0.04  $\mu m$  colloidal silica suspension, the initial microstructures of two titanium alloys were revealed by optical microscopy and secondary electron image (Zeiss EVO 15 LS Scanning Electron Microscope). The Ti6Al4V alloy consists of equiaxed  $\alpha$  phase distributed within  $\beta$  phase matrix, as can be seen in Fig. 1a, c. The near  $\alpha$  Ti3Al2.5V alloy is mainly characterized by equiaxed and acicular  $\alpha$  phases (Welsch et al., 1993), as shown in Fig. 1b, d. The specimens were machined and tested in the as-received condition.

### 2.3. Geometry and design of the specimen

The thin wall tubular specimens were manufactured from the supplied as 35 mm diameter rods. The geometry and dimension of the tubular specimen are shown in Fig. 2. Due to the geometry of the torsion specimen made out of the material bar, the available orientation to be identified is the axial direction along the material bar, as indicated by Peirs et al. (2011) and Verleysen and Peirs (2017). The flanges of the tubular specimen were designed to fit into matching hexagonal sockets in the mechanical testing apparatus. The same design of the torsion specimen was used for torsional tests from quasi-static to high strain rates.

### 2.4. Testing techniques

#### 2.4.1. Quasi-static torsion test

The quasi-static torsion tests were carried out by using a Zwick-Roell Z250 machine synchronized with IDS (Image Development Systems) UEye USB 3.0 Cameras<sup>1</sup> with high resolution image ( $2456 \times 2054$  pixels) at a frame rate of 1 fps. The gauge section of torsion specimen was spayed painted with black ink after the coating of white ink layer by using an airbrush. The shear strain of the specimen was directly measured from the gauge section using a commercial DIC software (Lavision DaVis)<sup>2</sup>. A Least-Squares Matching algorithm<sup>3</sup> (Pan et al., 2009) was used to process the images. The matching process was based on an affine shape function and a 6th order spline sub-pixel image interpolation scheme (GmbH, 2015). An area of rectangle is the region of interest for DIC analysis, as shown in Fig. 3. The engineering shear strain is determined from a 2 mm length shear gauge line at the center of gauge section. The slope of this shear gauge line provides a direct measurement of the shear strain. Note that a measurement uncertainty exists for the analysis of shear strain on a cylindrical surface using two dimensional DIC. The detailed strain analysis is demonstrated in Appendix A. It is found that the error is less than 1% in the range of shear strain values of interest in the present work. Consequently, no correction

<sup>1</sup> IDS Imaging Development Systems GmbH, Dimbacher Str. 6–8, 74,182 Obersulm, Germany.

<sup>2</sup> LaVisionUK Ltd, Victoria Road, Bicester OX26 6QB, United Kingdom.

<sup>3</sup> NorPix, Inc, 1751 Richardson Street, Suite 220, Montreal, Quebec, H3K 1G6 Canada.

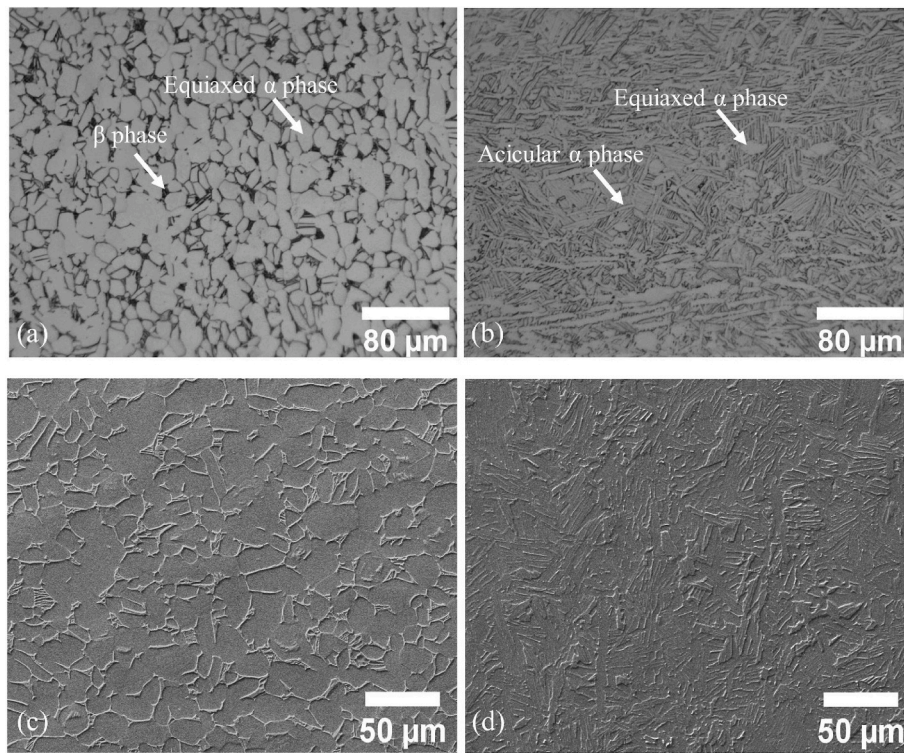


**Fig. 1.** Initial microstructures of two alloys investigated. Optical microscopy (a) Ti6Al4V alloy and (b) Ti3Al2.5V alloy. Secondary electron images (c) Ti6Al4V alloy and (d) Ti3Al2.5V alloy.

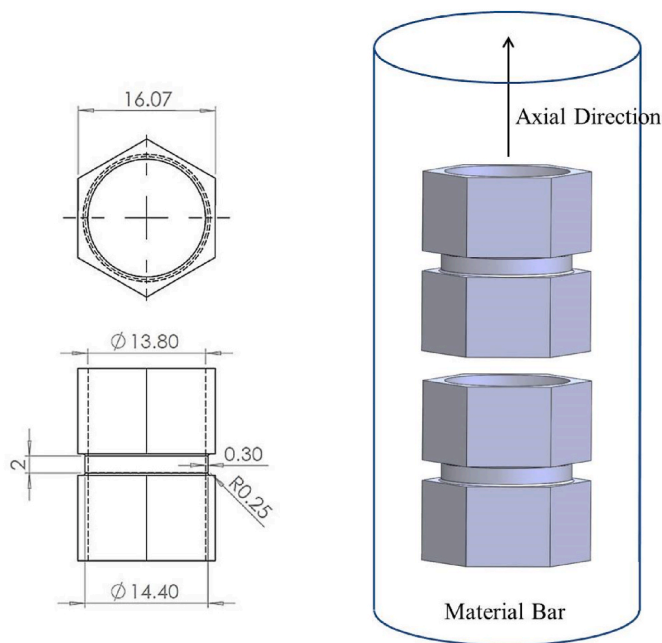


**Fig. 2.** Geometry and dimension of the specimen (Unit: mm). Torsion specimens were machined along the axial direction.

factor is employed in the shear strain from DIC analysis. Note that the measurement of engineering shear strain over the gauge length is similar to the methodology adopted by [Liao and Duffy \(1998\)](#) or [Fellows and Harding \(2001b\)](#). The current work is based on the distortion of the speckle pattern, while the latter is from the grid line on the cylindrical surface of gauge section.

The deformation process was monitored by a four camera system

with the angular separation between each camera being approximately  $90^\circ$ . The diagram of four cameras can be seen in [Fig. 4](#). The dot at the center of specimen indicates the axial direction. As also shown in [Fig. 3](#), the vertical direction of camera view is in the axial direction, and the horizontal direction of camera view is in the transverse direction. Four cameras were synchronized, and the images were recorded using a commercially available StreakPix software.<sup>3</sup> The speed of the screw driven crosshead was programmed to produce a constant angular velocity of 0.002 rad/s, which corresponds to a shear strain rate in the specimen of approximately 0.005/s.

#### 2.4.2. Medium strain rate testing

The medium strain rate tests were performed on a hydraulic Instron 8854 machine. The diagram is shown in [Fig. 5](#). The bespoke designed specimen fixtures were attached to the high speed rotary actuator and the load cell of the Instron machine. The torque signals were recorded by the Instron machine and an additional oscilloscope at an acquisition rate of 10,000 Hz. The upper part of the fixture and specimen rotated to the right during the test and the lower part was fixed. The optimized speed of the actuator was programmed to produce a nominal shear strain rate of approximately 10/s in the gauge section.

The shear deformation was recorded by a high speed Photron camera with image resolution of  $512 \times 296$  pixels at a framing rate of 10,000 fps. A K-type thermocouple was welded on the center of gauge section for the temperature measurement. A thermocouple junction was carefully produced by using TL-WELD Thermocouple Welder with argon gas. Next, the thermocouple junction was welded on the specimen by using PW500/CT2 Tweezer Micro Welder. The temperature was recorded by a TC-08 Thermocouple Data Logger (Pico Technology) with a resolution of  $0.025^\circ\text{C}$  and the fastest sampling rate available of about 67 Hz.

#### 2.4.3. High strain rate testing

The torsional split Hopkinson bar ([Fellows and Harding, 2001b](#); [Hou et al., 2000](#); [Macdougall and Harding, 1998, 1999](#); [Pellegrino et al., 2015](#)) was employed for the high strain rate torsion tests. [Fig. 6](#)



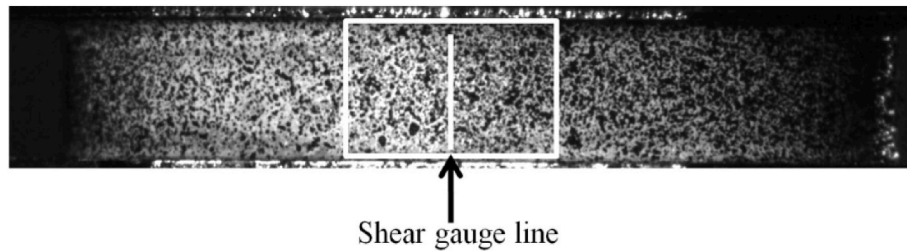


Fig. 3. An area of rectangle is the region of interest for DIC analysis. A shear gauge line is used for the measurement of shear strain of gauge section.

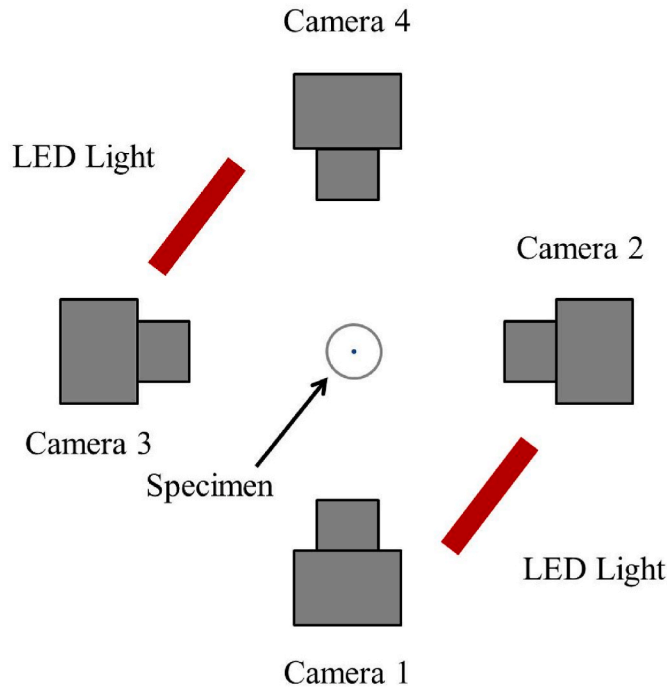


Fig. 4. Diagram of four camera distribution in quasi-static torsion test. The dot at the center of specimen indicates the axial direction.

schematically shows that the apparatus comprises input and output bars of 2.4 m in length and 25.4 mm in diameter. Both bars are made from Ti6Al4V alloy. This Hopkinson bar setup was used to achieve shear strain rates at the level of 1000/s. Two strain gauges 1 and 2 were bonded to the output and input bars respectively. The strain gauge signals were recorded by a Tektronix DPO 3034 digital oscilloscope. The high speed images, recorded using a Tamron SP60 mm Macro lens mounted on the high speed camera (Kirana camera), had a resolution of  $924 \times 748$  pixels, at a framing rate of  $2 \times 10^5$  fps and shutter speed 5 us. The high speed images were analyzed by DIC for a direct measurement of shear strain of gauge section.

Initially, the clamp was tightly holding the incident bar. The left end of the incident bar was rotated slowly to store the applied torque. As can be seen from the clamp system in Fig. 6, after the fracture of the high strength steel notch rod in the clamp, the stored torque was rapidly released, and the torque propagated along the bar toward the specimen. During dynamic deformation, Torque data  $T$  recorded by the strain gauge was converted into shear stress  $\tau$  according to

$$\tau = \frac{rT}{J} \quad (1)$$

where  $r$  is the average of inner and outer gauge section radii,  $J$  is the polar moment of inertia. A valid Hopkinson torsion bar tests require dynamic torque equilibrium at both ends of the torsion specimen. A

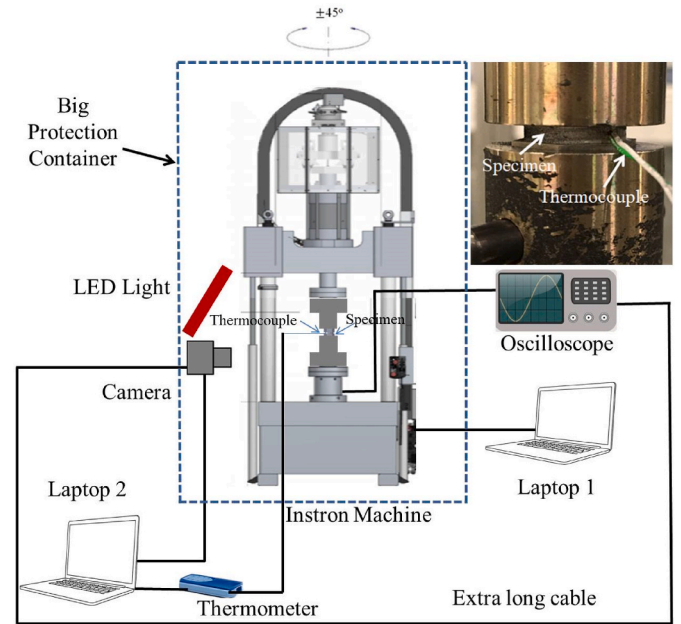


Fig. 5. Diagram of Hydraulic Instron 8854 setup for medium strain rate test.

typical incident and transmitted pulse from gauges are illustrated in Fig. 7a. A comparison of torques at two ends of specimen is shown in Fig. 7b, where Torque-in and Torque-out stand for the incident and transmitted torque, respectively. After a first period with the potential slack (Hou et al., 2000), dynamic torque equilibrium can be achieved in the plastic region. The torque from the transmitted side is used for the shear stress measurement of the specimen.

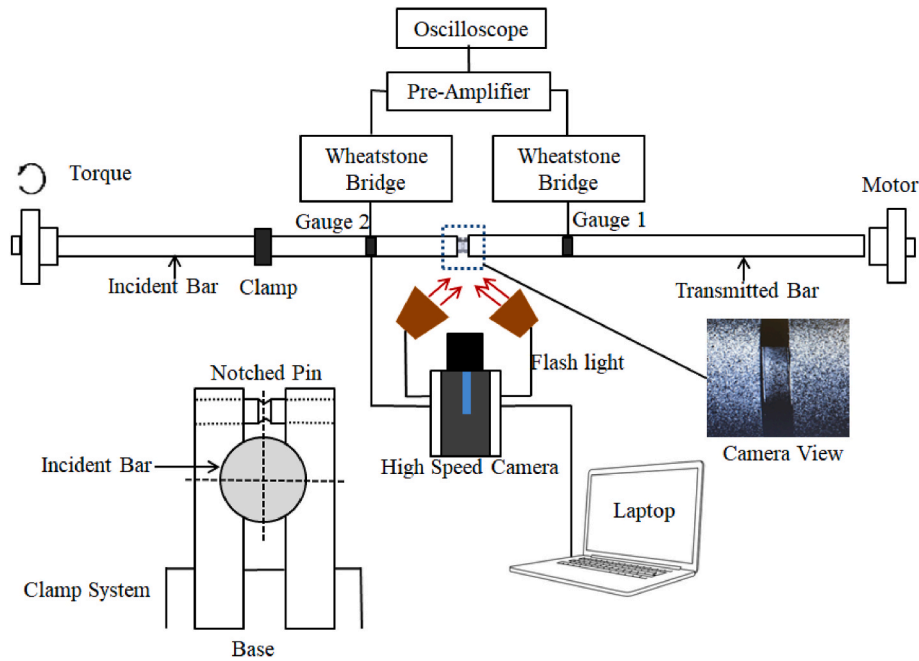
### 3. Results

#### 3.1. Quasi-static torsion test results

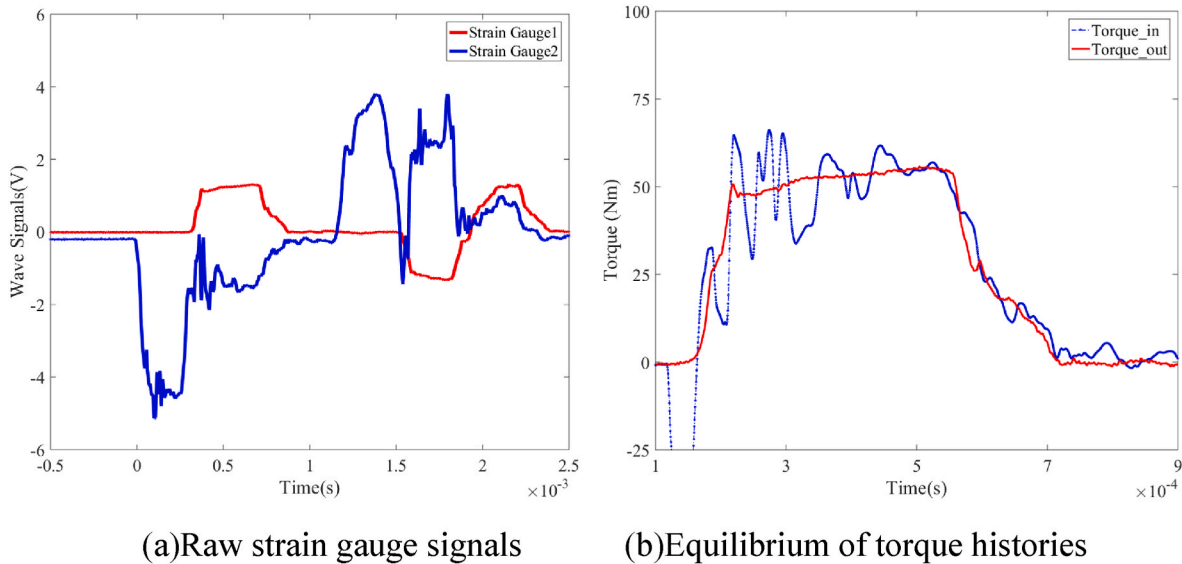
The shear strain around the circumference of gauge section is directly measured from DIC analysis. The shear stress is calculated from the global torque applied to the whole specimen recorded by the Zwick machine. From the shear stress and the corresponding shear strain histories from each camera recording in Fig. 8, the shear stress at the load drop point is at the time of approximately 28s for Ti6Al4V specimen. This test duration is shorter than the time of 127s for Ti3Al2.5V specimen. Here, the sudden load drop is marked by a black arrow, which indicates the failure initiation. The shear strain varies from 59% to 70% for Ti3Al2.5V specimen. The shear strain variation is between 8% and 10% for Ti6Al4V specimen. These results indicate some variations of the shear strain around the circumference of the torsion specimen.

Fig. 9(A)-a and Fig. 9B-a show the images from Camera 1 for Ti6Al4V alloy and Ti3Al2.5V alloy at the start of the test. The shear strain was measured at the center of gauge section through a shear gauge





**Fig. 6.** Schematic of TSHB apparatus, with a detailed diagram of the clamp system. The motor at the right end of transmitted bar is not connected. The image of the specimen attached to Hopkinson bar is shown from the camera view.



**Fig. 7.** Typical strain gauge signals recorded in high strain rate torsion test at 1200/s.

line function in the DIC software Lavision Davis. The slope of this shear gauge line provides a measurement of shear strain across the 2 mm gauge length of gauge section. The evolution of shear strain in percentage (the slope of shear gauge line) is shown in Fig. 9. The shear strain contour is engineering shear strain at each position from DIC analysis. The shear strain increases with the further distortion of the speckle pattern. The shear deformation of Ti3Al2.5V alloy is more apparent than that in Ti6Al4V alloy. The failure initiation corresponding to the load drop point in the shear stress history is highlighted by the arrows in the image Fig. 9A–d and Fig. 9B–d for two alloys. From the images with DIC analysis, the failure of both alloys locates at the region close to the end of gauge section. However, most of gauge section is in uniform shear deformation, which enables the measurement of shear strain and the following constitutive relationship of gauge section.

Fig. 10 shows the images from four cameras in the tests of Ti6Al4V

and Ti3Al2.5V specimens introduced in Figs. 8 and 9. One can find that the initiation of failure can be observed in the image from camera 1 or 2, however, it is not evident in the images taken at the same time from the other two cameras. This stage corresponds to the macro load drop point in the shear stress history from the Zwick machine shown in Fig. 8. Instead of a sudden separation of gauge section into two parts, the failure starts at some regions around the circumference. The test configuration with four cameras enables to identify the location of failure initiation and to measure the constitutive relationship at this failure initiation location.

Fig. 11 shows the shear stress-strain relationships of the two alloys from the four camera system under quasi-static condition. The initial elastic and plastic responses of the materials are consistent at four different locations up to the load drop point (failure initiation).

Table 2 compares the shear modulus and the yield stress (0.2%

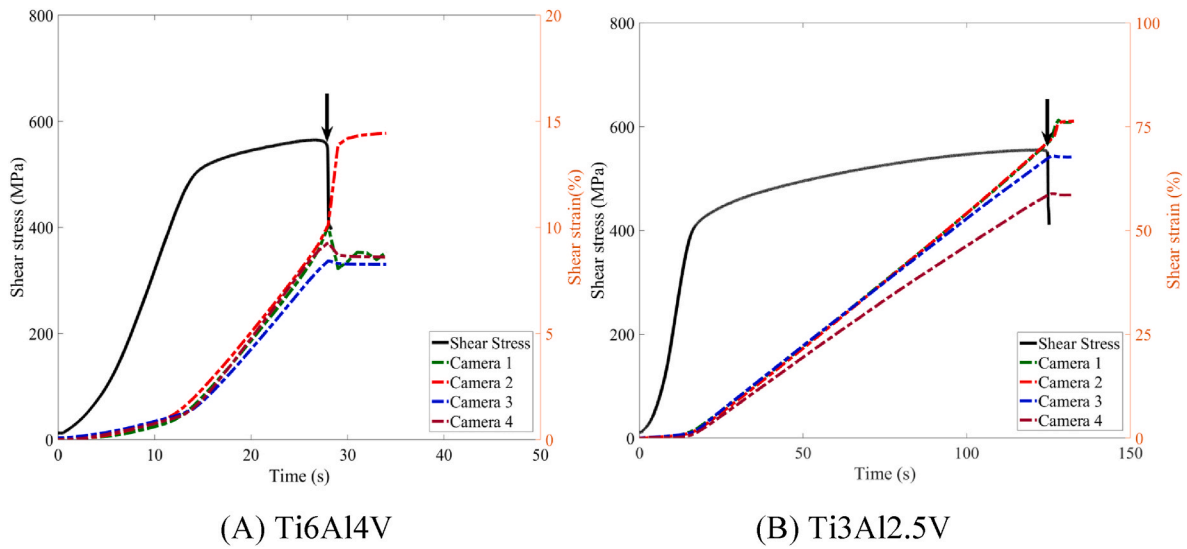


Fig. 8. Shear stress and strain histories for (A) Ti6Al4V alloy (B) Ti3Al2.5V alloy at quasi-static.

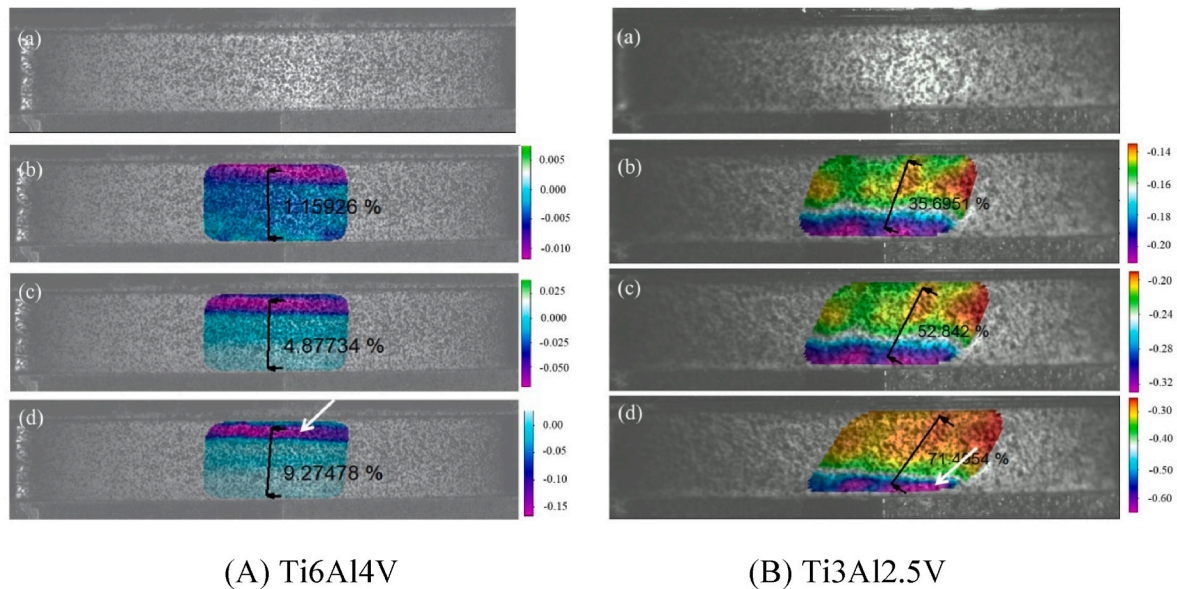


Fig. 9. Torsion deformation process for (A) Ti6Al4V alloy (B) Ti3Al2.5V alloy. The shear strain contour at each position from DIC analysis is shown. Different strain scales aim at a more straightforward observation of the strain evolution of two alloys.

offset) of both alloys from four camera locations. The shear modulus measured from the four camera system is consistent. The average shear modulus 40 GPa of Ti6Al4V alloy is slightly higher than 36 GPa of Ti3Al2.5V alloy. Regarding the 0.2% offset yield stress, the Ti3Al2.5V alloy shows an average yield stress of approximately 371 MPa, which is lower than the average yield stress of 474 MPa for Ti6Al4V alloy.

Table 3 summarizes the flow stress at a shear strain of 6% to quantitatively evaluate the similarity of the plastic flow in the shear stress-strain relationship from each camera location. The flow stress is in good agreement. Table 3 also compares different failure strains from each camera location. The failure strain values of Ti6Al4V alloy are 0.11 from camera 1 and 0.12 from camera 2, while the failure strain from camera 3 and 4 show the values of 0.10 and 0.11, indicating 10% variations among the failure strain measurements from four different locations. Likewise, the failure strain values of Ti3Al2.5V alloy are 0.70 from camera 1 or 2, which are higher than the failure strain 0.66 and 0.59 from camera 3 and 4. This indicates that there would be 10% variations of the failure strain from four cameras. Here, the global

failure strain from the Zwick machine is also compared. The average failure strain value 0.66 from the four camera system agrees with the global failure strain of 0.60 for Ti3Al2.5V alloy. The average failure strain value 0.11 from the four camera system is consistent with the global failure strain of 0.12 for Ti6Al4V alloy. Both alloys show 10% variations in the failure strain between the average measurement from four cameras and the global measurement from the Zwick machine. Comparison of the flow stress and failure strain in other tests is summarized in the tables in Appendix B. The variations ranging from 0 to 9% can be seen in the tests. The average failure strain from camera measurement is in good agreement with the global measurement from the Zwick machine.

The failure initiation can be identified with the assistance of recorded images. The local shear stress-strain relationship of two investigated alloys can be measured from the identified failure location. Table 4 summarizes the failure location from the four camera system. The local shear stress-strain response for each test is shown in Fig. 12. Note that this local shear stress-strain relationship is average engineering shear

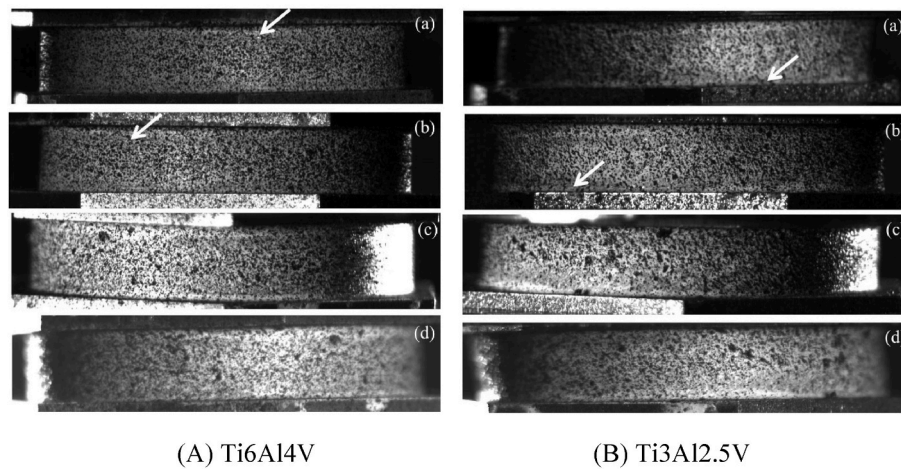


Fig. 10. Images at the onset of failure for (A) Ti6Al4V alloy and (B) Ti3Al2.5V alloy. The sequence of (a-d) corresponds to camera 1-4.

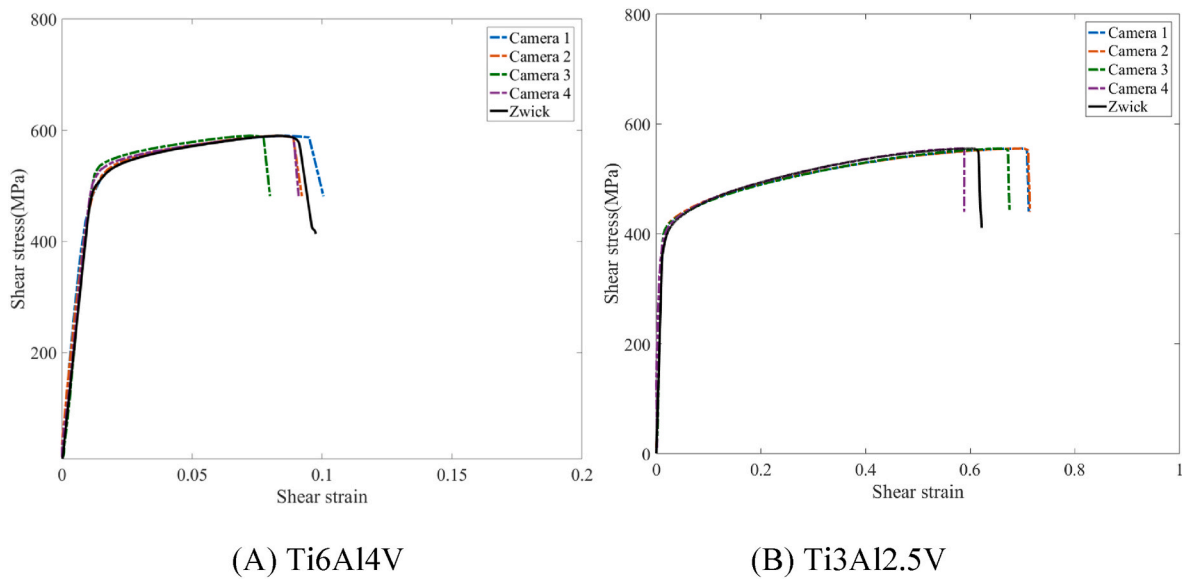


Fig. 11. Comparison among shear stress-strain relationships measured from four cameras and the Zwick machine for (A) Ti6Al4V alloy and (B) Ti3Al2.5V alloy.

Table 2

Comparison of the shear modulus and the yield stress (0.2% offset) for both alloys. The average values are given with the standard deviation.

| Camera   | Shear modulus (GPa) |           | 0.2% offset Yield (MPa) |           |
|----------|---------------------|-----------|-------------------------|-----------|
| Material | Ti6Al4V             | Ti3Al2.5V | Ti6Al4V                 | Ti3Al2.5V |
| Camera 1 | 40                  | 34        | 463                     | 358       |
| Camera 2 | 39                  | 38        | 463                     | 377       |
| Camera 3 | 40                  | 36        | 485                     | 377       |
| Camera 4 | 40                  | 37        | 485                     | 371       |
| Average  | 40 ± 0.5            | 36 ± 1.7  | 474 ± 12.7              | 371 ± 8.6 |

stress-strain relationship across the 2 mm gauge length in the area of gauge section where failure initiates. Ti6Al4V alloy shows higher flow stress than Ti3Al2.5V alloy. However, the failure strain in the range 0.10–0.12 for Ti6Al4V alloy, is significantly smaller than the failure strain between 0.57 and 0.70 for Ti3Al2.5V alloy. The investigation of the quasi-static torsion test using a four camera system aims at providing a better understanding of the torsion specimen. The constitutive relationships measured from different locations show consistent flow stress with a moderate variation of failure strain.

Table 3

Comparison of flow shear stress (at 0.06 shear strain) and failure strain of both alloys from the four camera system and the Zwick Machine. The average values from the four camera system are given with the standard deviation.

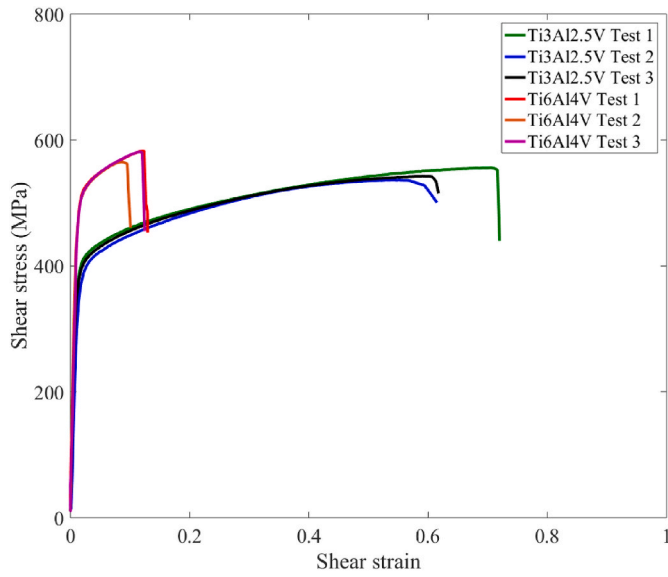
| Camera   | Flow Stress (MPa) |            | Failure strain |             |
|----------|-------------------|------------|----------------|-------------|
| Material | Ti6Al4V           | Ti3Al2.5V  | Ti6Al4V        | Ti3Al2.5V   |
| Camera 1 | 555               | 442        | 0.11           | 0.70        |
| Camera 2 | 556               | 443        | 0.12           | 0.70        |
| Camera 3 | 561               | 442        | 0.10           | 0.66        |
| Camera 4 | 556               | 443        | 0.11           | 0.59        |
| Average  | 557 ± 2.70        | 443 ± 0.57 | 0.11 ± 0.01    | 0.66 ± 0.07 |
| Zwick    | 554               | 440        | 0.12           | 0.60        |

Table 4

Shear failure strain at identified failure location for two alloys.

| Test     | Failure location |               | Failure strain |           |
|----------|------------------|---------------|----------------|-----------|
| Material | Ti6Al4V          | Ti3Al2.5V     | Ti6Al4V        | Ti3Al2.5V |
| Test 1   | Camera 2         | Camera 1 or 2 | 0.12           | 0.70      |
| Test 2   | Camera 1         | Camera 3      | 0.10           | 0.57      |
| Test 3   | Camera 1         | Camera 4      | 0.12           | 0.61      |





**Fig. 12.** Comparison of quasi-static shear stress-strain relationships of two alloys from identified failure initiation locations.

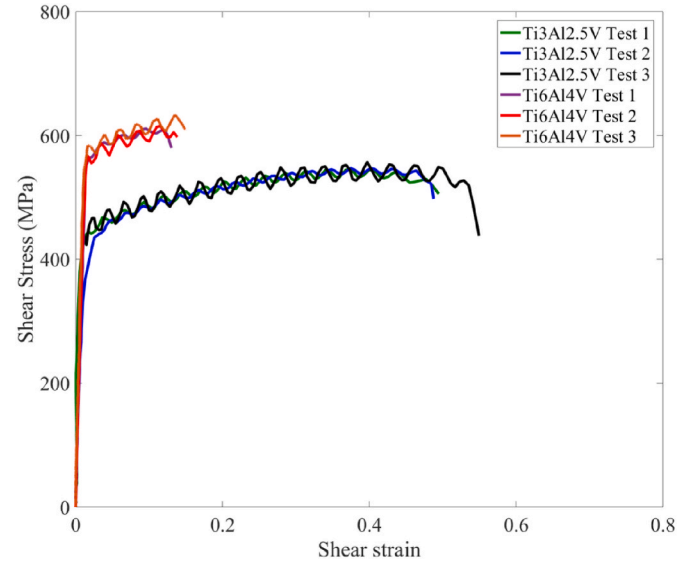
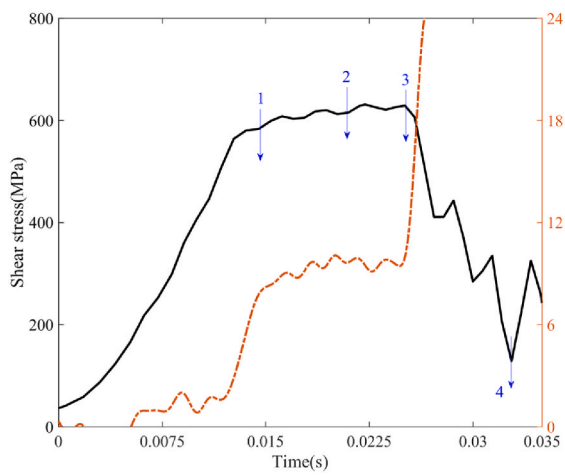
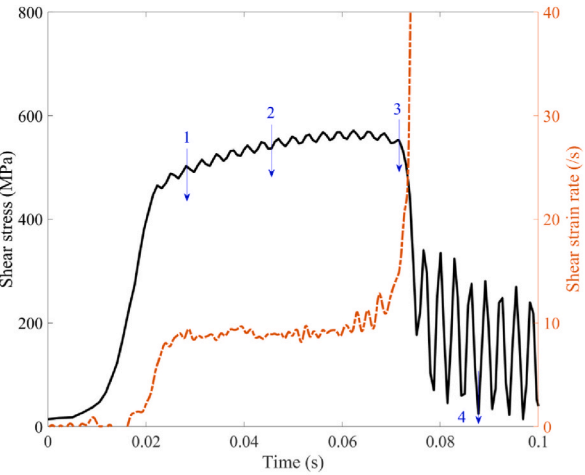


**Fig. 15.** Shear stress vs shear strain of Ti3Al2.5V and Ti6Al4V alloys at medium strain rate.



**(A) Ti6Al4V**



**(B) Ti3Al2.5V**

**Fig. 13.** Shear stress and shear strain rate histories at strain rate of 9/s for (A) Ti6Al4V alloy (B) Ti3Al2.5V alloy.

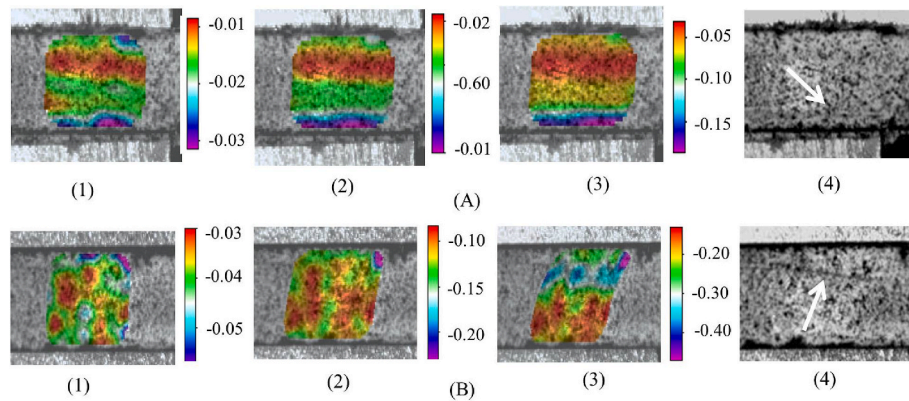


**Fig. 14.** Medium strain rate torsion deformation process (engineering shear strain is shown) corresponding to various stages in Fig. 13 for (A) Ti6Al4V alloy (B) Ti3Al2.5V alloy.

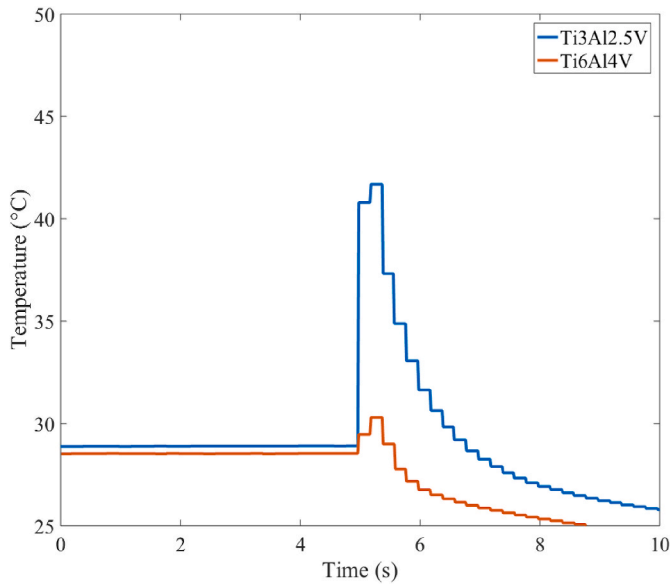


**Fig. 16.** Measurement of temperature evolution for two alloys at medium strain rate.

### 3.2. Medium strain rate torsion test results

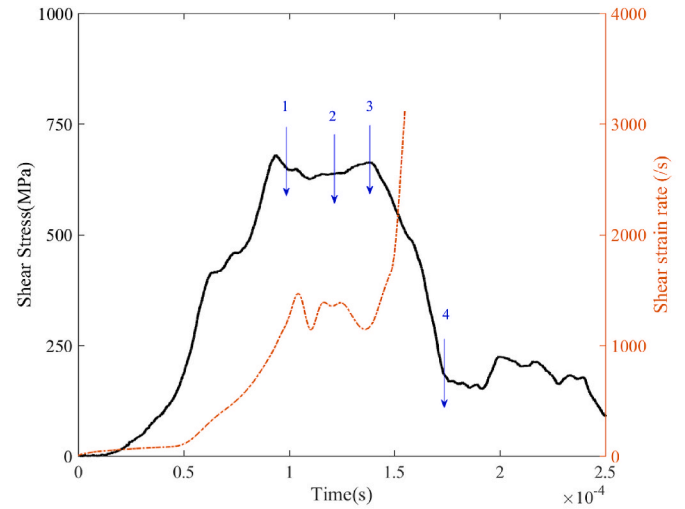
The torsion tests at medium strain rate were conducted on a fast Instron 8854 machine. Fig. 13 shows that the shear stress history from the Instron machine and the shear strain rate evolution from DIC analysis for two alloys. The specimens deform plastically at a constant strain rate of 9/s. The shear strain rate increases rapidly beyond the load drop at stage 3. Fig. 14 shows the corresponding deformation process from DIC analysis. The shear stress of Ti6Al4V alloy drops at the time of 0.025 s at stage 3, while the load drop of Ti3Al2.5V alloy appears at the time of 0.07 s at stage 3. Corresponding to the shear stress dropping to almost zero at stage 4, the specimens with cracks are marked by the white arrows in Fig. 14A(4) and Fig. 14B(4).

Fig. 15 compares the shear stress-strain responses for the two alloys investigated at medium strain rate. Both materials present consistent the shear stress-strain relationships. The failure strain of Ti6Al4V alloy is in the range between 0.12 and 0.15. This is lower than the failure strain of Ti3Al2.5V alloy which is between 0.48 and 0.52.

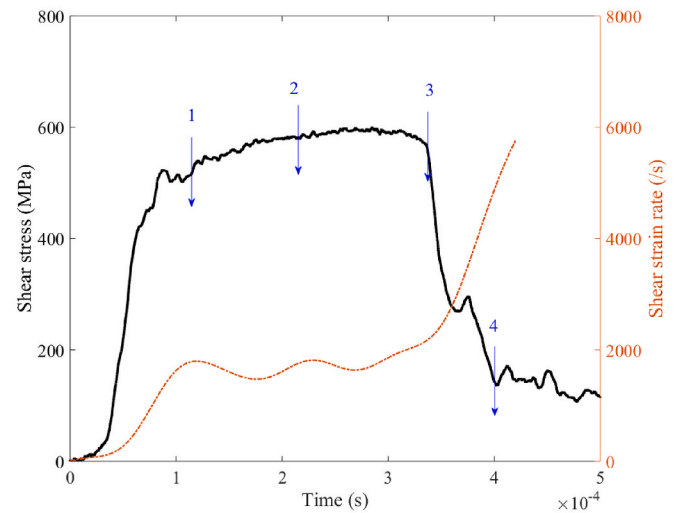
Typical temperature recordings at medium strain rate of 9/s are shown in Fig. 16. A maximum increase in the temperature from 28 °C to 30 °C can be observed for the Ti6Al4V alloy, while the temperature increases rapidly from 29 °C to 42 °C for the Ti3Al2.5V alloy. These are followed by temperature cooling down after the fracture of specimens. Note that this temperature measurement aims at giving a *general* indication of the temperature in the torsion specimen during medium strain rate deformation. The measured temperatures, at the level of several tens of degrees Celsius less than 100 °C, are impossible to cause any thermal softening effects for both alloys. Higher resolution thermocouple technique would be desirable to fully reveal the thermo-mechanical response (Macdougall, 2000; Rittel, 1999). The following microstructural analysis will provide further insight into the deformation and failure mechanisms at medium strain rate.

### 3.3. High strain rate torsion test results

Fig. 17 shows the dynamic shear stress as a function of time from TSHB, together with the corresponding shear strain rate history measured from DIC. The strain rate influences the strength and failure of a material. A constant strain rate torsion test is important to characterize these mechanical properties at high strain rates. The constant strain rates of 1260/s for Ti6Al4V alloy and 1600/s for Ti3Al2.5V alloy are



(A) Ti6Al4V alloy



(B) Ti3Al2.5V alloy

**Fig. 17.** Shear stress and shear strain rate histories for (A) Ti6Al4V alloy at strain rate of 1260/s (B) Ti3Al2.5V alloy at strain rate of 1600/s.

achieved during the plastic deformation up to the load drop point at stage 3. Subsequently, the shear strain rate of Ti3Al2.5V alloy increases rapidly at the time of 336 micro seconds. A dramatic increase in shear strain rate can be seen for Ti6Al4V alloy at the time of 139 micro seconds.

The high speed deformation process with DIC analysis at different stages for the two alloys is shown in Fig. 18. Corresponding to a sudden load drop at stage 3, the simultaneous photograph in Fig. 18A(3) presents the formation of intensive localized deformation marked by a white arrow for Ti6Al4V alloy. Dynamic localized shear deformation also occurs in Ti3Al2.5V alloy in Fig. 18B(3). The failure of Ti3Al2.5V alloy, observed from the high speed images and DIC analysis, is on a plane close to the center of gauge region. The failure of Ti6Al4V is close to the end of gauge section. These are followed by the final fracture of specimens in Fig. 18A (4) and Fig. 18B (4). The arrowed regions in the high speed images are for the following microstructural examination in Section 3.4.

The shear stress-strain responses at high strain rates for the two alloys investigated are compared in Fig. 19. The materials present consistent shear stress-strain relationship with a yield stress of approximately 620 MPa for Ti6Al4V alloy and 445 MPa for Ti3Al2.5V alloy.

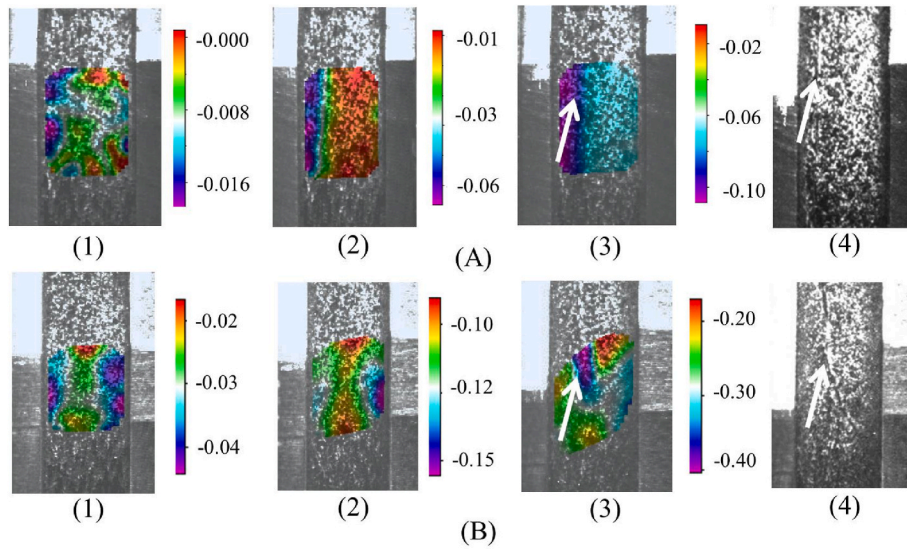


**Fig. 18.** High strain rate torsion deformation process (engineering shear strain field is shown) for (A) Ti6Al4V alloy and (B) Ti3Al2.5V alloy at different stages shown in Fig. 17.

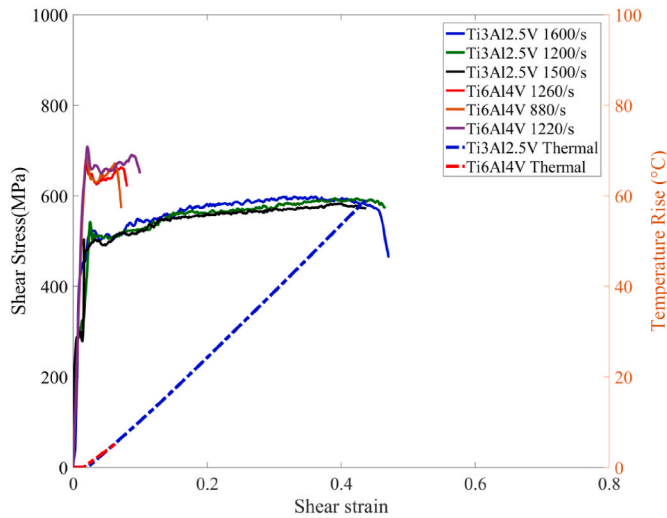


**Fig. 19.** Shear stress vs shear strain for high rate torsion tests for two alloys, together with the average calculated temperature rise.

The failure strain lies in the range of 0.41–0.46 for Ti3Al2.5V alloy and of 0.065–0.095 for Ti6Al4V alloy. Clearly, Ti3Al2.5V alloy shows a more ductile response than Ti6Al4V alloy. Due to the conversion of plastic work into heat, the dynamic deforming titanium alloys is associated with adiabatic temperature rise. With the assumption of adiabatic condition and the negligible thermoelastic coupling effect, the integration of the transient stress-thermal balance equation (Macdougall and Harding, 1999; Rittel, 1999; Rittel et al., 2017b) is as follows :

$$\beta_{int} \int_0^a \tau d\gamma_p = \rho c_p \Delta T \quad (2)$$

Here,  $\beta_{int}$  is the integral Taylor-Quinney factor,  $\rho$  is the density and  $c_p$  is the specific heat capacity of material,  $\Delta T$  is the temperature rise. The temperature rises for the high strain rate torsion tests are calculated, using the average Taylor-Quinney factors 0.4 for Ti6Al4V alloy and 0.6 for Ti3Al2.5V alloy, which represent typical experimentally measured values of the two alloys (Macdougall and Harding, 1998, 1999; Zhang et al., 2018) based on a transient infrared detector technique. The

average temperature rise up to the load drop shows a value of 6 °C for Ti6Al4V alloy, which is much lower than the value 60 °C for Ti3Al2.5V alloy. For the torsion tests being carried out at room temperature, the thermal softening effect on the dynamic constitutive relationship and dynamic shear failure are minimal for both alloys, particularly the Ti6Al4V alloy with very limited plastic deformation.

The dynamic shear stress-strain relationships of two alloys obtained from the fracture side facing the high speed camera are summarized in Fig. 20, together with the stress-strain relationships at quasi-static and medium strain rate. The yield stress of Ti6Al4V alloy increases from 470 MPa under quasi-static condition, 510 MPa at medium strain rate of 9/s and 620 MPa at high strain rates of 880–1260/s. The Ti3Al2.5V alloy (Zhang et al., 2021) shows an increasing yield stress from approximately 370 MPa, 400 MPa–445 MPa at quasi-static, medium strain rate of 9/s and high strain rates of 880–1600/s. Therefore, the strain rate has a significant effect on the shear yield stress. Considering the shear failure strain, the average failure strain of Ti3Al2.5V alloy decreases from 0.63 to 0.43 from quasi-static to high strain rates. The average failure strain of Ti6Al4V alloy decreases from 0.11 to 0.07 from quasi-static to high strain rates, with a slight increase to 0.15 at medium strain rate.

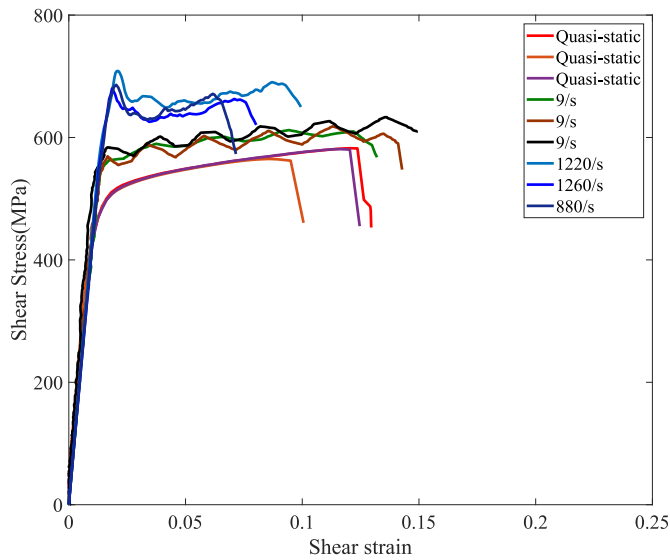
Together with the results at quasi-static and high strain rates, the medium strain rate data is important to reveal the evolution of shear stress as a function of shear strain rate. The Cowper-Symonds material model (Cowper and Symonds, 1957) is used to describe the strain rate dependence:

$$\tau = \tau_0 [1 + (\frac{\dot{\gamma}}{D})^{1/p}] \quad (3)$$

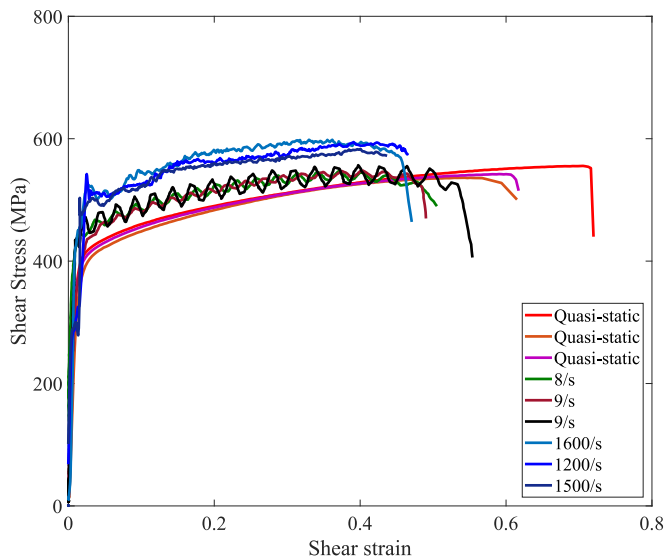
where  $\tau_0$  is the average shear stress at shear strain rate of 0.005/s,  $\dot{\gamma}$  is the shear strain rate,  $D$  and  $p$  are the parameters describing the strain rate sensitivity. At a given shear strain of 0.06, the shear stress values at strain rates from 0.005 to 1600/s are shown in Fig. 21 for two investigated alloys. The calibrated parameters are listed in Table 5. The Ti6Al4V alloy shows slightly higher strain rate sensitivity than Ti3Al2.5V alloy.

By using the Hopkinson torsion bar system, the present pure shear stress-strain relationship of Ti6Al4V alloy and the previous measurements (Macdougall and Harding, 1998, 1999) are compared in Fig. 22, together with the results from Peirs et al. (2011). Both the quasi-static and high strain rate shear stress-strain responses show very good agreement, except for the data of Peirs et al. (2011), with a slightly diverse elastic region.





(A) Ti6Al4V



(B) Ti3Al2.5V

**Fig. 20.** Comparison of shear stress-strain relationships of two alloys from quasi-static to high strain rates.

The current pure shear constitutive response and the shear compressive behavior of Ti3Al2.5V alloy (Zhang et al., 2018, 2020b) using SCS or compression specimen are compared in Fig. 23. Here, the equivalent shear stress-strain relationship can be transferred from the available constitutive relationships from SCS or compression. According to von Mises theory, the shear stress  $\tau = \sigma_{true}/\sqrt{3}$  and the shear strain  $\gamma = \sqrt{3}\epsilon_{true}$  can be obtained from the equivalent true stress-strain relationship of SCS or compression specimen. A first observation is the less oscillation in the pure shear stress-strain curves from torsion tests. The dynamic yield stress values are similar of approximately 450 MPa using different specimens. At a given shear strain of 0.26 and comparable strain rates, the flow stress from SCS is 663 MPa. This is higher than the flow stress of 585 MPa from the torsion test at shear strain rates of 1200–1500/s. The flow stress from SCS or compression increases apparently with the increasing strain. This trend is different from that in dynamic pure stress-strain relationship.

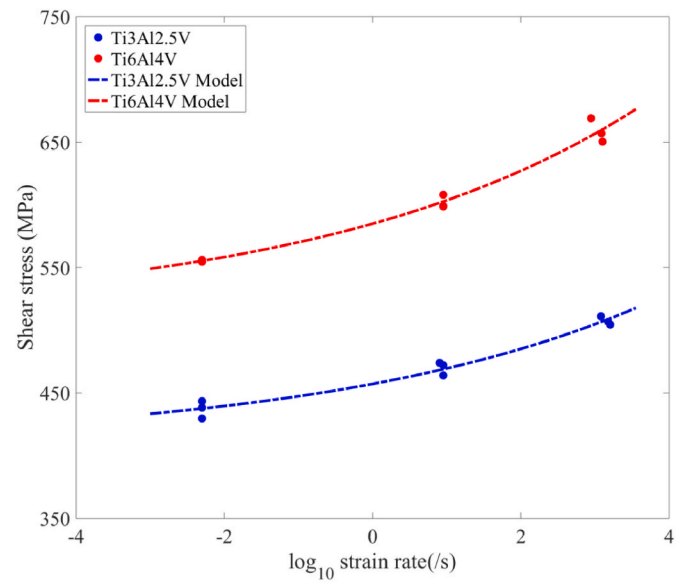


**Fig. 21.** The shear stress of two alloys as a function of logarithmic shear strain rate at a given shear strain of 0.06.

**Table 5**

Constants in Cowper-Symonds material model.

| Material  | D        | p      |
|-----------|----------|--------|
| Ti6Al4V   | 3.3216E8 | 9.9943 |
| Ti3Al2.5V | 2.016E9  | 9.9433 |

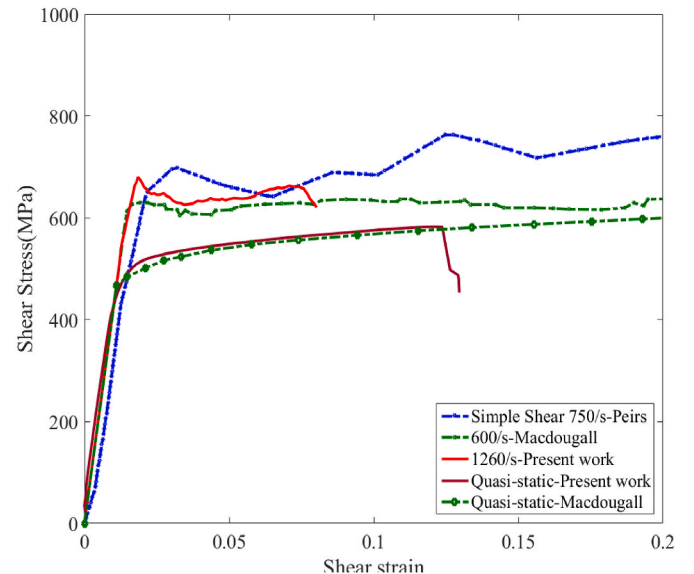


**Fig. 22.** Comparison of the pure shear stress-strain relationships of Ti6Al4V alloy between the present work and the previous measurement (MacDougall and Harding, 1998, 1999). The simple shear stress-strain data from the literature (Peirs et al., 2011) is also compared.

### 3.4. Microstructural characterization

Optical microscopy (OM) and scanning electron microscopy (SEM) are used to characterize the fractured microstructures of these two alloys. Fig. 24a-b and Fig. 24(d-e) show that the microstructure undergoes shear deformation for Ti6Al4V and Ti3Al2.5V alloys at quasi-static and medium strain rate. No localization can be seen ahead of a crack tip

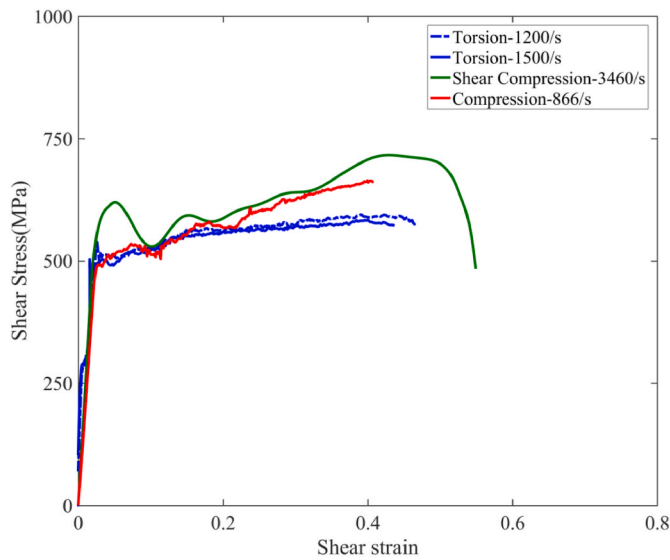


Fig. 23. Comparison of dynamic shear stress-shear strain relationship of Ti3Al2.5V alloy from torsion, SCS and compression.

(white dash circle) in Fig. 24e in Ti3Al2.5V alloy during medium strain rate deformation. However, Figs. 24c and e show adiabatic shear bands (arrowed) in the fractured Ti6Al4V and Ti3Al2.5V specimens loaded at high strain rates. The ASB locates at the region where the macro strain localization is observed in the high speed images in Fig. 18. The microstructures adjacent to ASB are heavily elongated along the shear direction, illustrating the highly localized character of their dynamic shear failure mechanism.

For Ti3Al2.5V alloy, Fig. 25 shows the SEM image for the microstructure around the crack tip in Fig. 24e. The microstructure along the crack is shown in Fig. 25b. Instead of a shear localization band, the voids (arrowed) distribute ahead of the crack tip in Fig. 25a. Voids can also be observed along two edges of crack in Fig. 25b. Likewise, Fig. 25c shows the magnified microstructure with voids (arrowed) adjacent to the fracture surface for Ti6Al4V alloy at medium strain rate. This is different from the shear band (dashed arrow) characteristic in Ti6Al4V alloy at high strain rate (Fig. 25d).

Fracture mechanisms were examined by SEM. The quasi-static fracture surfaces of Ti6Al4V and Ti3Al2.5V specimens present apparent voids and cracks (white square) in Fig. 26a and Fig. 26d. At medium strain rate, Figs. 26b and e show the SEM fractograph of the fracture specimens, which are characterized by similar but larger voids (white square) along the shear direction. These fractographic observations agree with the failure mechanism with void growth and coalescence shown in Fig. 24 (b, e) and Fig. 25(a–c). As suggested by Liao and Duffy (1998) in their quasi-static torsion test, the nucleation of voids is driven by the critical shear plastic strain of titanium alloys. It is believed that no real possibility of thermal softening exists in quasi-static torsion. The medium rate torsion is associated with a certain amount of temperature rise. The similar fracture surfaces indicate that failure at quasi-static and medium strain rate results from a void growth induced process.

Compared to the fractograph of specimens at quasi-static and medium strain rate, dimples (white arrowed) surrounded by severe shear facets are observed in the fracture surface of the Ti6Al4V and Ti3Al2.5V specimens at high strain rates in Fig. 26c and f. These observations are similar to the previous microstructural characterizations for Ti6Al4V alloy (Liao and Duffy, 1998; Rittel and Wang, 2008; Zhou et al., 1996). Fig. 20 shows that the shear failure strain of both alloys decreases from quasi-static to high strain rates. The localized deformation within ASB results in the earlier failure of materials at high strain rates than the quasi-static and medium strain rate. Fig. 27 shows a closer look at the fracture surfaces of Ti6Al4V alloy and Ti3Al2.5V alloy at high strain

rates. Compared to the (macro) brittle Ti6Al4V alloy with evenly distributed and slightly elongated dimples, the fractograph of the ductile Ti3Al2.5V alloy presents more significantly elongated dimples and severe shear characteristics.

#### 4. Discussion

Most of the previous studies of the torsion tests were limited to Ti6Al4V alloy at high strain rates or quasi-static loading. This paper compares the pure shear flow and the failure of Ti6Al4V alloy and Ti3Al2.5V alloy from quasi-static to high strain rates using bespoke techniques. These two alloys are conceived for the design of fan containment and fan blade in aircraft jet engine (Rolls-Royce plc, 2015) respectively, to improve the structural impact resistance in events, such as the blade off and bird strike. The relationship between fan blade and fan containment is like spear and shield. The fan blade possesses high strength, while the fan containment component is of lower strength for easier manufacture process, but higher ductility in order to absorb impact energy from the released fan blade during impact events. The development of high strength fan blade requires the simultaneous development of fan containment with high ductility. The biaxial stress ratio of  $-1$  in the torsion test and the zero stress triaxiality can reveal the inherent plastic flow response of a material. The corresponding image analysis provides real time strain measurements in pure shear deformation. The measured shear stress-strain relationships show significant rate dependence. The Ti6Al4V alloy presents much higher yield stress than that in Ti3Al2.5V alloy, while the latter shows higher failure strain. The observed and estimated temperature rises are relatively more apparent in Ti3Al2.5V alloy than Ti6Al4V alloy at medium strain and high strain rates. The pure shear constitutive relationship in the present work will support the analysis of impact events in aircraft engineering applications. More importantly, the proposed bespoke torsion techniques will guide the material testing for constitutive relations of current and future developed impact resistant alloys.

Four camera system was constructed to monitor the entire specimen gauge section under quasi-static condition. The flow stress in the constitutive relationship from the Zwick machine data agrees with DIC measurements. However, this global shear stress-strain measurement cannot capture the localised failure strain. With the current four camera system, a measurement of shear stress-strain relationship can be obtained at the failure initiation location. The shear modulus, yield stress and failure strain of Ti3Al2.5V alloy are compared to those of Ti6Al4V alloy. Although the Ti3Al2.5V alloy shows lower flow stress than Ti6Al4V alloy, the failure strain in the range of  $0.57$ – $0.70$  is significantly larger than the failure strain between  $0.10$  and  $0.12$  for Ti6Al4V alloy. There are some variations in the strain distribution around the circumference of the specimen, which may be due to the difficulties (Fellows and Harding, 2001b) in machining the specimen, alignment of the test fixture and specimen, and material inconsistencies. One may argue that an uneven change of shear stress would exist around the circumference. The shear stress of torsion specimen is the average shear stress around the circumference of gauge section. The flow stress in the stress-strain curves from four camera system agrees with that in the global stress-strain curve from the Zwick machine. This indicates the reasonable use of average shear stress around the circumference of gauge section. One important issue is about the orientation of torsion specimen. The current torsion specimen was made from a material bar. Similar to the torsion specimen of Peirs et al. (2011) and Verleysen and Peirs (2017), the only available orientation which can be identified is the axial direction along the material bar. A torsion specimen made from a plate with marked orientations, as indicated by Revil-Baudard et al. (2015) and Ruiz de Sotillo et al. (2021), would be helpful in the future, in order to study the potential effect of orientation on the failure initiation around the circumference of torsion specimen.

Although the bespoke four camera system promotes the understanding of torsion specimen, currently it was not possible to employ a

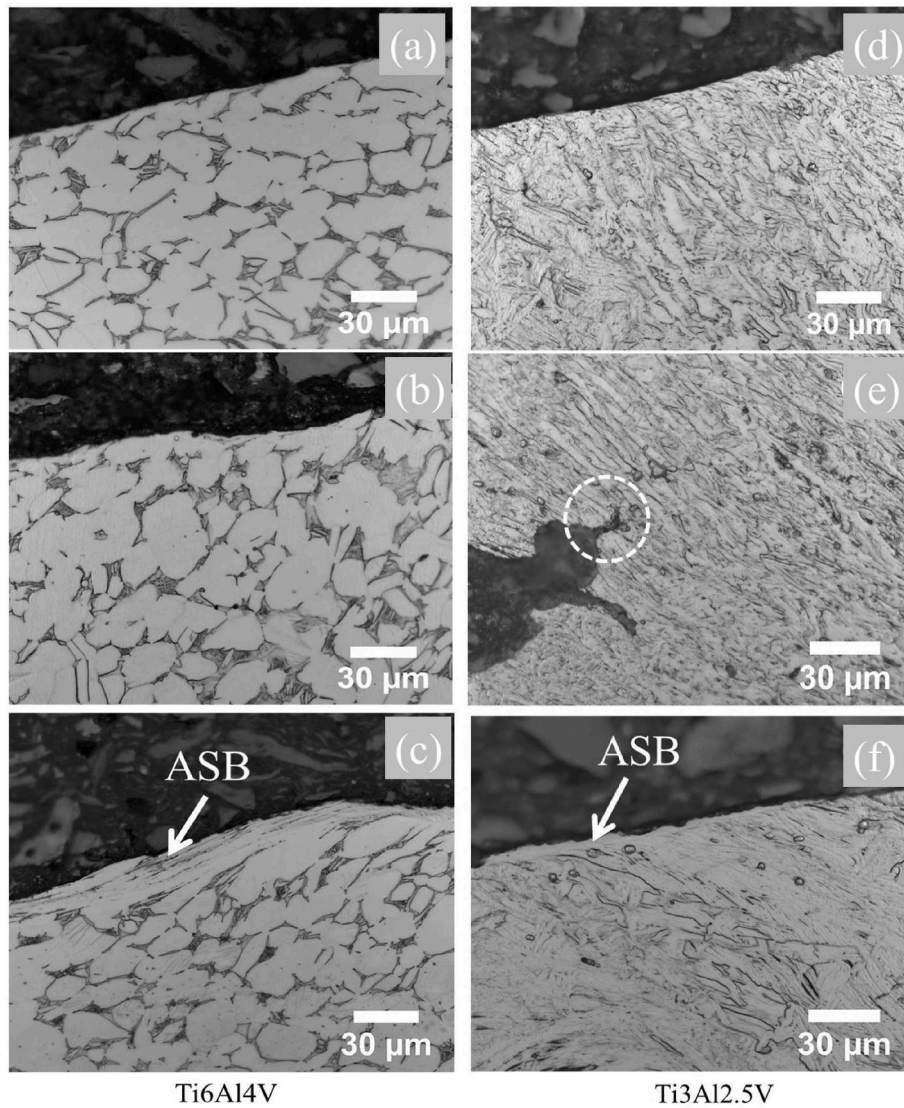


**Fig. 24.** OM images of microstructures of the Ti6Al4V alloy (a–c) from quasi-static, medium strain rate 9/s to high strain rate 1260/s, and Ti3Al2.5V alloy (d–f) from quasi-static, medium strain rate 9/s to high strain rate 1600/s.

four camera system for the medium and high strain rate tests, due to the space limitation and the availability of equipment. Note that the pure shear stress-strain curves are consistent at different locations from the four camera system (Fig. 11). It's believed that valuable results at medium and high strain rates can still be obtained with one camera system, as can be seen in the torsion test carried out by Liao and Duffy (1998). The medium strain rate torsion test is rarely reported in the literature. Here, the medium strain rate tests were carried out at a constant strain rate of about 9/s by using a bespoke designed fixture on the fast hydraulic Instron machine. Several initial attempts were made to achieve medium strain rates of 50–100/s, however, the torque data from the sensor fixed on the base of the hydraulic Instron machine shows significant oscillations. This is due to the elastic response and the inertia of the system (Bhujangrao et al., 2020). By gradually reducing the speed of rotary actuator, an optimized strain rate is designed to be about 10/s with only a slight oscillation in the shear stress-strain relationship. The temperature measurement was carried out in order to provide a general indication of the temperature at medium strain rate. The monitored temperatures about several tens of degrees Celsius in Ti3Al2.5V alloy and Ti6Al4V alloy are believed to be quite modest. Only several degrees Celsius temperature rise is observed for Ti6Al4V alloy. Consequently, the temperature cannot cause any thermal softening effects during

medium rate torsional deformation. A thermocouple technique with higher resolution (Macdougall, 2000; Rittel, 1999) would be required to reveal more detailed information of the thermomechanical behaviour at medium strain rate. The microstructures deformed at medium strain rate are examined in Fig. 24b, e and Fig. 25a–c. No localized shear band is observed ahead of the crack tip. The fracture surfaces are similar to those under quasi-static condition. This also indicates the role of temperature is not significant at medium strain rate.

The Campbell Hopkinson torsion bar was employed for torsion tests at high strain rates. Constant shear strain rates from 800 to 1600/s can be achieved when the specimen enters the plastic flow stage. Dynamic deformation process was recorded by a high speed camera. The shear stress-strain relationships at high strain rates show good repeatability and agree with the previous results (Macdougall and Harding, 1998, 1999) using the TSHB technique. The estimated temperature rises at high rate torsion tests up to load drop is approximately 60 °C for Ti3Al2.5V alloy, which is higher than the 6 °C in Ti6Al4V alloy. This indicates the minimum thermal softening effect in the torsional constitutive response of both alloys, particularly for Ti6Al4V alloy with almost no plastic deformation and negligible adiabatic temperature rise. Only after the shear localization would the temperature increase dramatically to several hundred degrees, according to the experimental



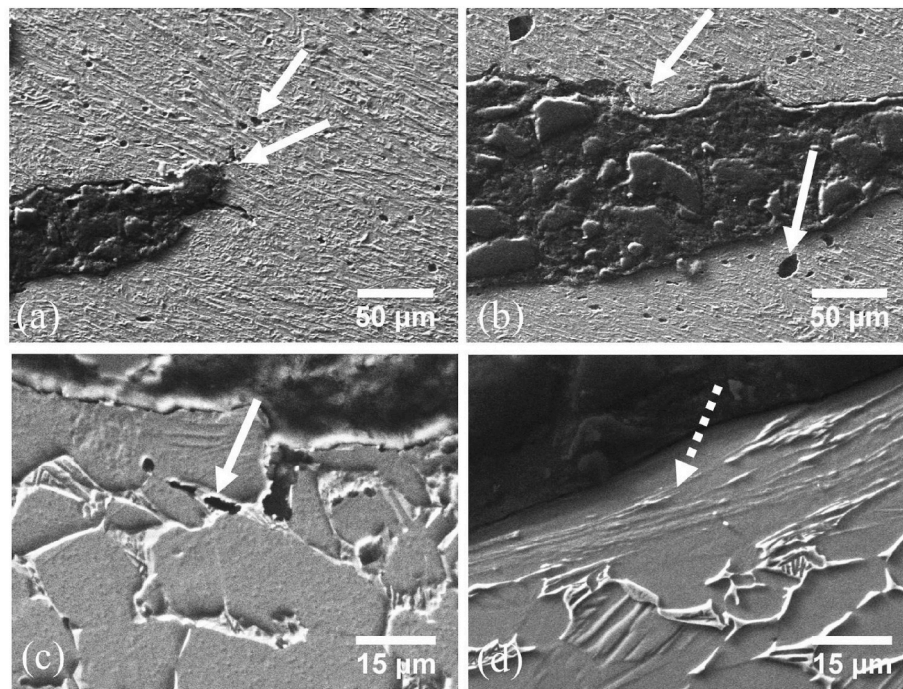


**Fig. 25.** SEM images for the microstructures around the crack for Ti3Al2.5V alloy at medium strain rate (a–b), and Ti6Al4V alloy at medium and high strain rates (c–d).

measurements across two decades for Ti6Al4V alloy (Macdougall and Harding, 1998, 1999; Rittel and Wang, 2008), and recently for Ti3Al2.5V alloy (Zhang et al., 2018). The significant temperature rise is the outcome of the intensive strain localization rather than becoming its prerequisite. Considering the potential geometrical effect (Fellows and Harding, 2001a; Liao and Duffy, 1998; Molinari and Clifton, 1987; Rittel et al., 2008b) or microstructural localization effect (Rittel et al., 2008a, 2017a), this could lead to non-uniform strain in the specimen, localized deformation and the subsequently locally higher temperature. Fracture mechanisms at high strain rates are characterized by localized shear bands and the elongated dimples surrounded by severe shear facets for Ti3Al2.5V alloy and Ti6Al4V alloy. Compared to the ductile Ti3Al2.5V alloy with evenly distributed elongated dimples and severe shear surface, the fractograph of the relatively brittle Ti6Al4V alloy shows less elongated dimples and less severe shear characteristics. These observed fracture surfaces at high strain rate are similar to the dynamic shear fracture mechanisms in the literature (Liao and Duffy, 1998; Ramesh, 2002; Rittel and Wang, 2008). The failure of both titanium alloys at quasi-static of  $10^{-3}$ /s and high strain rate of  $10^3$ /s results from a void growth induced process. Compared to the quasi-static loading, the adiabatic shear band causes the earlier failure of material at high strain rates. Although the shear deformation at medium strain rate of  $10^1$ /s is with a certain amount of temperature rise, the microstructural analysis shows that the failure mechanism is closer to that at quasi-isothermal test rather than high strain rate test. As a precursor of failure and fracture at high strain rates, the shear band promotes the failure of titanium alloys, a point recently highlighted by Longère and Dragon (2015).

It is found that the pure shear stress-strain behavior of Ti6Al4V alloy in the present work shows good agreement with the simple shear stress-strain relationship in the literature. In addition, the shear constitutive responses of Ti3Al2.5V alloy measured from the torsion and SCS or compression are compared based on the von Mises theory. The dynamic yield stress values are comparable at comparable strain rates, however, the flow stress from SCS significantly increases with the increasing strain. This is different from the lower strain hardening characteristic in dynamic shear stress-strain relationship from torsion. Each type of specimen has its unique advantage. The combined use of SCS and torsion

specimens would be desirable to fully characterize the shear behavior of materials under different stress states. The strain rate dependence and strain hardening would vary at different high strain rates in torsion tests. The range of achievable strain rates using the current torsion Hopkinson bar is about 500–2000/s. The strain rate effect and strain hardening effect in this strain region would not change significantly.

Future research will continue the investigation of the thermo-mechanical pure shear response of the lightweight aircraft alloys at medium and high strain rates, using a multiple-camera system and an infrared camera technique. A reduced length of gauge section and an improved clamp system to store higher torque would allow the characterization of pure shear at higher strain rates from several 1000/s up to 10,000/s. This will also be the next step in the development of bespoke torsion techniques.

## 5. Conclusion

This paper compares the pure shear constitutive responses of Ti6Al4V alloy and Ti3Al2.5V alloy using bespoke torsion techniques. Compared to Ti3Al2.5V alloy, Ti6Al4V alloy presents higher flow stress and rate dependence with lower failure strain. Generally, the failure strain for both alloys decreases with increasing rates from quasi-static 0.005/s to high strain rates of about 1000/s. The material deformation and failure at quasi-static loading are monitored by a four camera system, which enables the measurement of shear modulus, yield stress and flow behavior at the location of failure initiation. Torsion tests of Ti6Al4V and Ti3Al2.5V alloys at medium strain rate of 9/s are carried out to connect the relationships of pure shear flow and failure between quasi-static and high strain rates. The measured temperatures for Ti6Al4V and Ti3Al2.5V alloys are modest during medium strain rate deformation. A comparison of the present results and the literature shows that the dynamic pure shear stress-strain relationships agree with the simple shear stress-strain relationships, while the strain hardening in pure shear would be lower than that from SCS or compression. Both Ti6Al4V and Ti3Al2.5V alloys fail by localized deformation within the shear band at high strain rates. This indicates that shear band can occur in both ductile alloy and brittle alloy with almost no plastic deformation

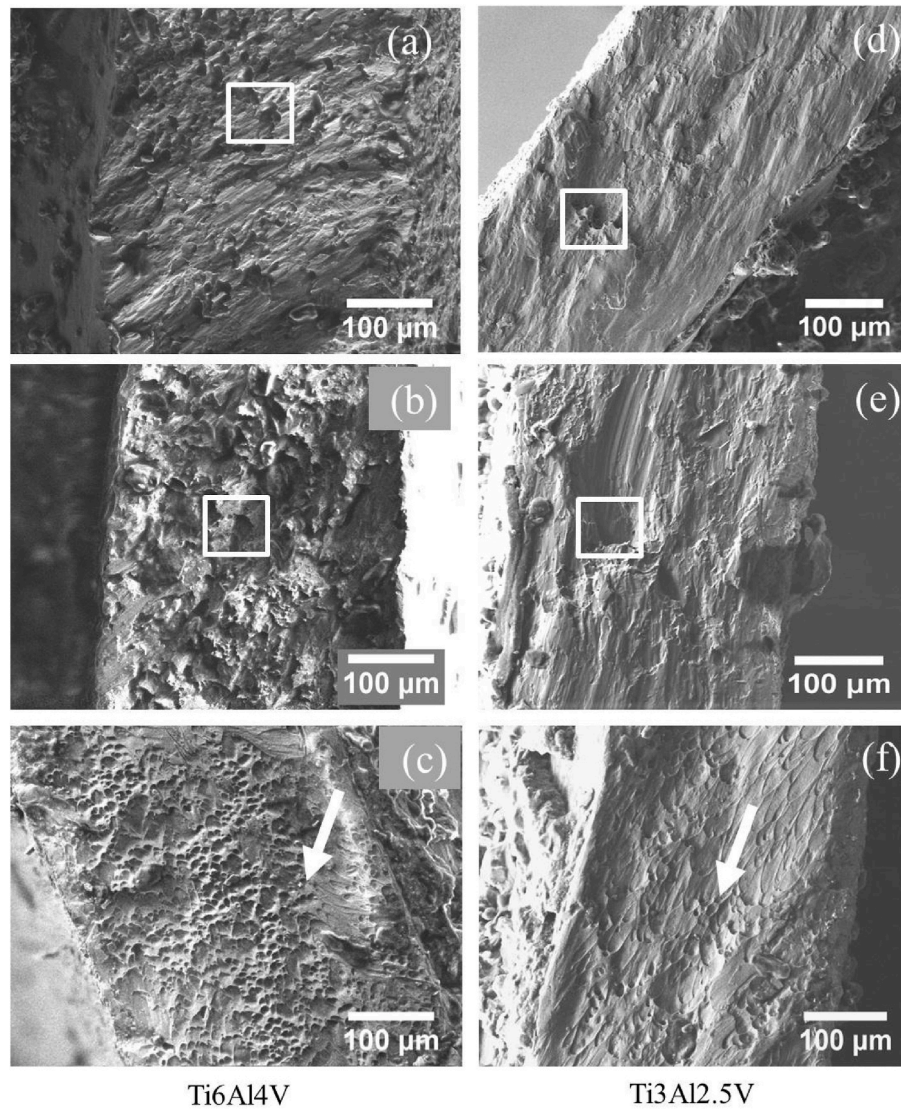


**Fig. 26.** SEM images of fracture surface of Ti6Al4V alloy (a–c) from quasi-static, medium to high strain rate, and Ti3Al2.5V alloy (d–f) from quasi-static, medium to high strain rate.

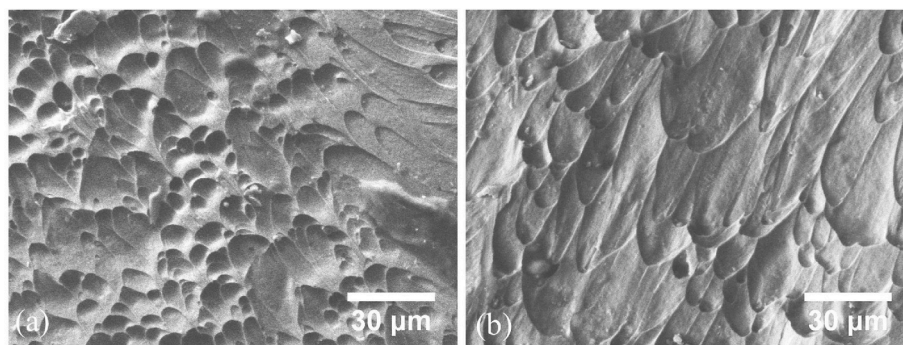


**Fig. 27.** High magnification SEM image of the fracture surfaces of (a) Ti6Al4V alloy and (b) Ti3Al2.5V alloy at high strain rates.

and almost no temperature rise before the final collapse. Different from the failure with localized shear band at high strain rates, the material failure is a void growth induced process at medium strain rate and at quasi-isothermal condition.

#### Author statement

**Longhui Zhang:** Conceptualization, Investigation, Methodology, Visualization, Writing – original draft, Writing – review & editing. **David Townsend:** Investigation, Methodology, Writing – review & editing. **Antonio Pellegrino:** Resource. **Nik Petrinic:** Resource

## Declaration of competing interest

The authors declare that they have no known competing financial interests or personal relationships that could have appeared to influence the work reported in this paper. Correspondence and request can be addressed to Dr. Longhui Zhang.

## Acknowledgements

The authors thank Mr. J. Fullerton, Dr. M. Rutherford, Mr. S. Carter,

Mrs. K. Bamford and Dr. K. Dragnevski for their assistance. We thank Dr. DAS. Macdougall and Dr. J. Reed from Rolls-Royce plc for the continuous support in the development of torsion technique, and the discussion about thermomechanics. Prof. D. Rittel and Dr. A. Dorogoy at the Technion are acknowledged for the guidance of the SCS technique. Critical comments and fruitful suggestions from Dr. S. Walley at The Cavendish Laboratory about the physics of torsion are greatly appreciated.

## Appendix A

During shear deformation, the shear strain from cylindrical gauge section is projected onto a flat image plane in the DIC imaging system. As can be seen in Fig. A1, a movement on the image plane from the location a to b, which is horizontal over a length  $L$ , corresponds to the surface travels with the rotation angle  $\theta$  through an arc  $S$  (location c to location d).

The shear strain in the image plane from DIC analysis is

$$\gamma_{plane} = \frac{L}{l} \quad (A.1)$$

The shear strain from the cylinder analysis is

$$\gamma_{cylinder} = \frac{R\theta}{l} \quad (A.2)$$

where  $L = R \sin \theta$ ,  $l$  is the length of gauge section.

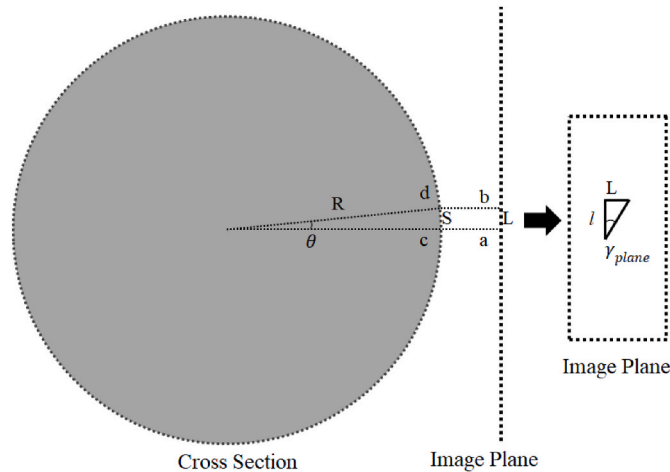


Fig. A1. Schematic of a circular cross section through a specimen gauge, and the corresponding shear strain measurement in the image plane

Fig. A2 compares the shear strain on the cylinder surface and image plane. The error between two shear strain values increases to 0.7% at shear strain of 0.75 from the cylinder surface. Within the shear strain range of interest, no correction was made to the measured DIC strain in the present work. The engineering shear strain measurement directly from the gauge section in the present work, is similar to the measurements of Fellows and Harding (2001b) or Liao and Duffy (1998). The former is based on the distortion of the speckle pattern, while the latter is from the grid line applied to the surface of the torsion specimen.



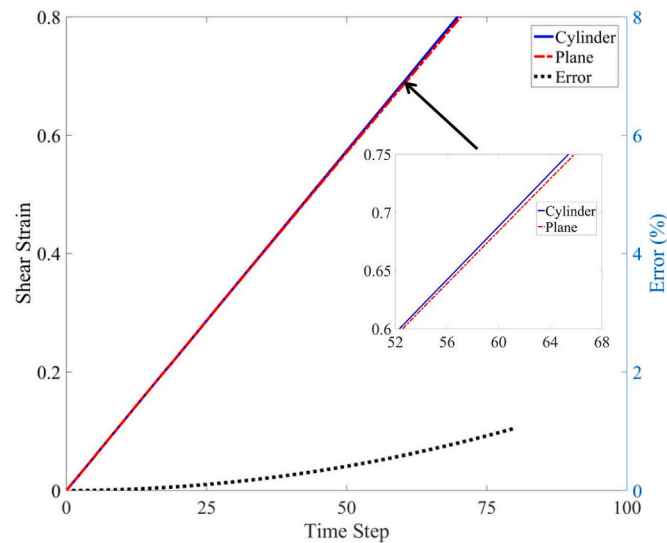


Fig. A2. Comparison of shear strain between cylinder surface and DIC image plane.

## Appendix B

**Table B1**

Comparison of flow shear stress (at 0.06 shear strain) from the four camera system and the Zwick Machine in quasi-static torsion tests. The average values of flow stress from 4 camera system are given with the standard deviation.

| Camera   | Flow Stress (MPa) |            |            |           |            |            |
|----------|-------------------|------------|------------|-----------|------------|------------|
|          | Test 1            |            | Test 2     |           | Test 3     |            |
| Material | Ti6Al4V           | Ti3Al2.5V  | Ti6Al4V    | Ti3Al2.5V | Ti6Al4V    | Ti3Al2.5V  |
| Camera 1 | 555               | 442        | 555        | 437       | 560        | 438        |
| Camera 2 | 556               | 443        | 556        | 437       | 558        | 436        |
| Camera 3 | 561               | 442        | 561        | 430       | 562        | 438        |
| Camera 4 | 556               | 443        | 556        | 437       | 556        | 438        |
| Average  | 557 ± 2.70        | 443 ± 0.57 | 557 ± 2.70 | 435 ± 3.5 | 559 ± 2.58 | 438 ± 1.00 |
| Zwick    | 554               | 440        | 554        | 435       | 556        | 439        |

**Table B2**

Comparison of failure strain from the four camera system and the Zwick Machine in quasi-static torsion tests. The average values of failure strain from 4 camera system are given with the standard deviation.

| Camera   | Failure Strain |             |             |             |             |             |
|----------|----------------|-------------|-------------|-------------|-------------|-------------|
|          | Test 1         |             | Test 2      |             | Test 3      |             |
| Material | Ti6Al4V        | Ti3Al2.5V   | Ti6Al4V     | Ti3Al2.5V   | Ti6Al4V     | Ti3Al2.5V   |
| Camera 1 | 0.11           | 0.70        | 0.10        | 0.50        | 0.10        | 0.55        |
| Camera 2 | 0.12           | 0.70        | 0.09        | 0.50        | 0.11        | 0.58        |
| Camera 3 | 0.10           | 0.66        | 0.08        | 0.57        | 0.10        | 0.57        |
| Camera 4 | 0.11           | 0.59        | 0.09        | 0.54        | 0.12        | 0.61        |
| Average  | 0.11 ± 0.01    | 0.66 ± 0.07 | 0.09 ± 0.01 | 0.53 ± 0.04 | 0.11 ± 0.01 | 0.58 ± 0.03 |
| Zwick    | 0.12           | 0.60        | 0.09        | 0.49        | 0.11        | 0.54        |

## References

- Baker, W.E., Yew, C., 1966. Strain-rate Effects in the Propagation of Torsional Plastic Waves.
- Bhujangrao, T., Froustey, C., Iriondo, E., Veiga, F., Darnis, P., Mata, F.G., 2020. Review of intermediate strain rate testing devices. *Metals* 10, 894.
- Campbell, J., Dowling, A., 1970. The behaviour of materials subjected to dynamic incremental shear loading. *J. Mech. Phys. Solid.* 18, 43–63.
- Cowper, G.R., Symonds, P.S., 1957. Strain-hardening and strain-Rate Effects in the Impact Loading of Cantilever Beams, vol. 28. Brown Univ. Tech. Rept.
- Daly, S., Rittel, D., Bhattacharya, K., Ravichandran, G., 2009. Large deformation of nitinol under shear dominant loading. *Exp. Mech.* 49, 225–233.
- Dodd, B., Bai, Y., 2012. *Adiabatic Shear Localization: Frontiers and Advances*. Elsevier.
- Dorogoy, A., Rittel, D., Godinger, A., 2015. Modification of the shear-compression specimen for large strain testing. *Exp. Mech.* 1–13.
- Duffy, J., Campbell, J.D., Hawley, R.H., 1971. On the use of a torsional split Hopkinson bar to study rate effects in 1100-0 aluminum. *J. Appl. Mech.* 38, 83–91.
- Espinosa, H., Patanella, A., Fischer, M., 2000. A novel dynamic friction experiment using a modified Kolsky bar apparatus. *Exp. Mech.* 40, 138–153.
- Farren, W., Taylor, G., 1925. The heat developed during plastic extension of metals. In: *Proceedings of the Royal Society of London A: Mathematical, Physical and Engineering Sciences*. The Royal Society, pp. 422–451.

- Fellows, N.A., Harding, J., 2001a. Localization of plastic deformation during high strain rate torsion testing of rolled homogeneous armour. *J. Strain Anal. Eng. Des.* 36, 197–210.
- Fellows, N.A., Harding, J., 2001b. Use of high-speed photography to study localisation during high-strain-rate torsion testing of soft iron. *Mater. Sci. Eng., A* 298, 90–99.
- GmbH, L., 2015. Product-Manual for DaVis 8.3: Imaging Tools. LaVision GmbH Göttingen.
- Hopkinson, B., 1914. A method of measuring the pressure produced in the detonation of high explosives or by the impact of bullets. *Proceedings of the Royal Society of London. Series A* 89, 411–413.
- Hou, J.P., Ruiz, C., Trojanowski, A., 2000. Torsion tests of thermosetting resins at impact strain rate and under quasi-static loading. *Mater. Sci. Eng., A* 283, 181–188.
- Kolsky, H., 1949. An investigation of the mechanical properties of materials at very high rates of loading. *Proc. Phys. Soc. B* 62, 676.
- Lewis, J., Campbell, J., 1972. The development and use of a torsional Hopkinson-bar apparatus. *Exp. Mech.* 12, 520–524.
- Leyens, C., Peters, M., 2003. *Titanium and Titanium Alloys: Fundamentals and Applications*. John Wiley & Sons.
- Li, P., Siviour, C.R., Petrinic, N., 2009. The effect of strain rate, specimen geometry and lubrication on responses of aluminium AA2024 in uniaxial compression experiments. *Exp. Mech.* 49, 587–593.
- Liao, S., Duffy, J., 1998. Adiabatic shear bands in a Ti-6Al-4V titanium alloy. *J. Mech. Phys. Solid.* 46, 2201–2231.
- Longère, P., Dragon, A., 2015. Dynamic vs. quasi-static shear failure of high strength metallic alloys: experimental issues. *Mech. Mater.* 80, 203–218. Part B.
- Lu, F., Lin, Y., Wang, X., Lu, L., Chen, R., 2015. A theoretical analysis about the influence of interfacial friction in SHPB tests. *Int. J. Impact Eng.* 79, 95–101.
- Macdougall, D., 2000. Determination of the plastic work converted to heat using radiometry. *Exp. Mech.* 40, 298–306.
- Macdougall, D., Harding, J., 1998. The measurement of specimen surface temperature in high-speed tension and torsion tests. *Int. J. Impact Eng.* 21, 473–488.
- Macdougall, D., Harding, J., 1999. A constitutive relation and failure criterion for Ti6Al4V alloy at impact rates of strain. *J. Mech. Phys. Solid.* 47, 1157–1185.
- Molinari, A., Clifton, R.J., 1987. Analytical characterization of shear localization in thermoviscoplastic materials. *J. Appl. Mech.* 54, 806–812.
- Nicholas, T., Campbell, J., 1972. Shear-strain-rate effects in a high-strength aluminum alloy. *Exp. Mech.* 12, 441–447.
- Pan, B., Asundi, A., Xie, H., Gao, J., 2009. Digital image correlation using iterative least squares and pointwise least squares for displacement field and strain field measurements. *Opt. Laser. Eng.* 47, 865–874.
- Peirs, J., Verleysen, P., Degrieck, J., 2011. Experimental Study of the High Strain Rate Shear Behaviour of Ti6Al4V, *Applied Mechanics and Materials*. Trans Tech Publ, pp. 130–135.
- Pellegrino, A., Tagarielli, V.L., Gerlach, R., Petrinic, N., 2015. The mechanical response of a syntactic polyurethane foam at low and high rates of strain. *Int. J. Impact Eng.* 75, 214–221.
- Ramesh, K., 2002. Effects of high rates of loading on the deformation behavior and failure mechanisms of hexagonal close-packed metals and alloys. *Metall. Mater. Trans.* 33, 927–935.
- Ranc, N., Taravella, L., Pina, V., Herve, P., 2008. Temperature field measurement in titanium alloy during high strain rate loading—adiabatic shear bands phenomenon. *Mech. Mater.* 40, 255–270.
- Revil-Baudard, B., Cazacu, O., Flater, P., Kleiser, G., 2015. Plastic deformation of high-purity  $\alpha$ -titanium: model development and validation using the Taylor cylinder impact test. *Mech. Mater.* 80, 264–275.
- Rittel, D., 1999. On the conversion of plastic work to heat during high strain rate deformation of glassy polymers. *Mech. Mater.* 31, 131–139.
- Rittel, D., Landau, P., Venkert, A., 2008a. Dynamic recrystallization as a potential cause for adiabatic shear failure. *Phys. Rev. Lett.* 101, 165501.
- Rittel, D., Lee, S., Ravichandran, G., 2002. A shear-compression specimen for large strain testing. *Exp. Mech.* 42, 58–64.
- Rittel, D., Silva, M., Poon, B., Ravichandran, G., 2009. Thermomechanical behavior of single crystalline tantalum in the static and dynamic regime. *Mech. Mater.* 41, 1323–1329.
- Rittel, D., Wang, Z., 2008. Thermo-mechanical aspects of adiabatic shear failure of AM50 and Ti6Al4V alloys. *Mech. Mater.* 40, 629–635.
- Rittel, D., Wang, Z., Dorogoy, A., 2008b. Geometrical imperfection and adiabatic shear banding. *Int. J. Impact Eng.* 35, 1280–1292.
- Rittel, D., Zhang, L., Osovski, S., 2017a. Mechanical characterization of impact-induced dynamically recrystallized nanophase. *Physical Review Applied* 7, 044012.
- Rittel, D., Zhang, L.H., Osovski, S., 2017b. The dependence of the Taylor–Quinney coefficient on the dynamic loading mode. *J. Mech. Phys. Solid.* 107, 96–114.
- Rolls-Royce plc, 2015. *The Jet Engine*. John Wiley & Sons.
- Ruiz de Sotomayor, M., Doquet, V., Longère, P., Papasidero, J., 2021. Anisotropic, rate-dependent ductile fracture of Ti-6Al-4V alloy. *Int. J. Damage Mech.* 0 (0), 1–29.
- Siviour, C.R., Walley, S.M., 2018. Inertial and Frictional Effects in Dynamic Compression Testing, the Kolsky-Hopkinson Bar Machine. Springer, pp. 205–247.
- Taylor, G.I., Quinney, H., 1934. The latent energy remaining in a metal after cold working. *Proc. Roy. Soc. Lond.: Mathematical, Physical and Engineering Sciences* 143, 307–326.
- Tresca, H., 1879. Sur la fluidité et l'écoulement des corps solides. *Annales du conservatoire des arts et métiers*, 4.
- Tzibula, S., Lovinger, Z., Rittel, D., 2018. Dynamic tension of ductile polymers: experimentation and modelling. *Mech. Mater.* 123, 30–42.
- Verleysen, P., Peirs, J., 2017. Quasi-static and High Strain Rate Fracture Behaviour of Ti6Al4V.
- Walley, S., 2007. Shear localization: a historical overview. *Metall. Mater. Trans.* 38, 2629–2654.
- Welsch, G., Boyer, R., Collings, E.W., 1993. *Materials Properties Handbook: Titanium Alloys*. ASM international.
- Winter, R., 1975. Adiabatic shear of titanium and polymethylmethacrylate. *Phil. Mag.* 31, 765–773.
- Yang, G., Song, Y., 1985. The TSHB technique for material testing at high rates of strain. *Appl. Math. Mech.* 6 (5), 393–399.
- Yang, R., Zhang, H., Shen, L., Xu, Y., Bai, Y., Dodd, B., 2014. A modified split Hopkinson torsional bar system for correlated study of  $\tau$ - $\gamma$  relations, shear localization and microstructural evolution. *Phil. Trans. Roy. Soc. Lond.: Mathematical, Physical and Engineering Sciences* 372, 20130208.
- Zhang, L., Pellegrino, A., Townsend, D., Petrinic, N., 2020a. Strain rate and temperature dependent strain localization of a near  $\alpha$  titanium alloy. *Int. J. Impact Eng.* 145, 103676.
- Zhang, L., Pellegrino, A., Townsend, D., Petrinic, N., 2020b. Thermomechanical constitutive behaviour of a near  $\alpha$  titanium alloy over a wide range of strain rates: experiments and modelling. *Int. J. Mech. Sci.* 189, 105970.
- Zhang, L., Rittel, D., Osovski, S., 2018. Thermo-mechanical characterization and dynamic failure of near  $\alpha$  and near  $\beta$  titanium alloys. *Mat Sci Eng a-Struct* 729, 94–101.
- Zhang, L., Townsend, D., Petrinic, N., Pellegrino, A., 2021. Measurement of pure shear constitutive relationship from torsion tests under quasi-static, medium, and high strain rate conditions. *J. Appl. Mech.* 88 (12), 121003.
- Zhou, M., Rosakis, A.J., Ravichandran, G., 1996. Dynamically propagating shear bands in impact-loaded prenotched plates—I. Experimental investigations of temperature signatures and propagation speed. *J. Mech. Phys. Solid.* 44, 981–1006.